DISSERTATIONES
PHYSICAE
UNIVERSITATIS
TARTUENSIS
121

MARKO ELTERMANN

Analysis of samarium doped TiO2 optical and multiresponse oxygen sensing capabilities

DISSERTATIONES PHYSICAE UNIVERSITATIS TARTUENSIS
121

DISSERTATIONES PHYSICAE UNIVERSITATIS TARTUENSIS
121

MARKO ELTERMANN

Analysis of samarium doped TiO_2 optical and multiresponse oxygen sensing capabilities

UNIVERSITY OF TARTU
Press

The study was carried out at the Institute of Physics, University of Tartu, Estonia.

The dissertation was admitted on June 11, 2019 in partial fulfilment of the requirements for the degree of Doctor of Philosophy in Physics, and was allowed for defence by the Council of the Institute of Physics, University of Tartu.

Supervisors: Dr. Sven Lange, University of Tartu, Estonia
Dr. Raivo Jaaniso, University of Tartu, Estonia

Opponent: Dr. Krisjanis Smits, University of Latvia, Latvia

Defense: August 30, 2019, University of Tartu, Estonia

Publication of this thesis was financially supported by Graduate School of Functional materials and technologies receiving funding from the European Regional Development Fund in University of Tartu, Estonia.

ISSN 1406-0647
ISBN 978-9949-03-083-5 (print)
ISBN 978-9949-03-084-2 (pdf)

University of Tartu Press
www.tyk.ee

CONTENTS

LIST OF PUBLICATIONS

Base publications of the thesis

I. **M. Eltermann**, K. Utt, S. Lange, and R. Jaaniso, "Sm^{3+} doped TiO_2 as optical oxygen sensor material," *Optical Materials*, vol. 51, pp. 24–30, Jan. 2016. https://doi.org/10.1016/j.optmat.2015.11.020

II. L. Dolgov, **M. Eltermann**, S. Lange, V. Kiisk, L. Zhou, J. Shi, M. Wu, and R. Jaaniso, "Au/SiO_2 nanoparticles in TiO_2:Sm^{3+} films for improved fluorescence sensing of oxygen," *Journal of Materials Chemistry C*, vol. 5, no. 45, pp. 11958–11964, 2017. https://doi.org/10.1039/C7TC03704J

III. **M. Eltermann**, V. Kiisk, A. Berholts, L. Dolgov, S. Lange, K. Utt, and R. Jaaniso, "Modeling of luminescence-based oxygen sensing by redox-switched energy transfer in nanocrystalline TiO_2:Sm^{3+}," *Sensors and Actuators B: Chemical*, vol. 265, pp. 556–564, Jul. 2018. https://doi.org/10.1016/j.snb.2018.03.034

IV. **M. Eltermann**, V. Kiisk, S. Lange, R. Jaaniso, "Multivariable oxygen sensing based on photoconductivity and intrinsic/extrinsic photoluminescence of TiO_2 nanoparticles," submitted to *Sensors and Actuators B: Chemical*, Apr. 2019

Author's contribution

I. Preparation of samples, optical and gas sensing experiments, mathematical modelling, preparation of the manuscript.
II. Optical and gas sensing experiments.
III. Preparation of samples, optical and gas sensing experiments, preparation of the manuscript.
IV. Preparation of samples, optical, electrical and gas sensing experiments, mathematical modelling, preparation of the manuscript.

Other publications

1. L. Puust, V. Kiisk, **M. Eltermann**, H. Mändar, R. Saar, S. Lange, I. Sildos, Leonid Dolgov, L. Matisen, and R. Jaaniso, "Effect of ambient oxygen on the photoluminescence of sol–gel-derived nanocrystalline ZrO_2:Eu,Nb," *J. Phys. D: Appl. Phys.*, vol. 50, no. 21, p. 215303, 2017. https://doi.org/10.1088/1361-6463/aa6c48
2. T. Tikk, T. Paara, **M. Eltermann**, A. Krumme, R. Jaaniso, V. Kiisk, and S. Lange, "TiO_2:Sm^{3+} based luminescent oxygen sensitive probes in LDPE packaging material," *Proceedings of the Estonian Academy of Sciences*, vol. 66, no. 4, p. 450, 2017. https://doi.org/10.3176/proc.2017.4.16

ABBREVIATIONS

SEM	scanning electron microscope
CCD	charge-coupled device
PMT	photomultiplier tube
MFC	mass flow controller
EC	electrical conductance
PL	photoluminescence
PLI	photoluminescence intensity
RE	rare earth
UV	ultraviolet
IR	infrared
FET	field-effect transistor
RET	resonant energy transfer
PAH	polycyclic aromatic hydrocarbon
BET method	Brunauer, Emmett and Teller method

1. INTRODUCTION

1.1. Motivation

Years of research and development have taken us to the point where an artificial sensor is much better at making measurements than a human. Temperature, wind velocity, acceleration, force etc. are just some of the many examples. The advantages of sensors over humans are obvious. However, odour sensing is a category where sensors still lag behind humans and particularly other mammals, such as dogs, explaining the ongoing efforts in gas sensor development.

Inorganic metal oxide semiconductor materials, in spite of years of research, remain in the focus of gas sensor development because of their very simple construction, low cost and ability to survive in harsh environments. Although they have difficulties in differentiating the vast number of organic molecules associated with biological processes around us, they excel in detecting simple yet common gases such as oxygen, hydrogen, carbon monoxide, water vapour, nitrogen oxides, ozone etc. Many of these gases are important pollutants, explosive or toxic.

While traditional sensor designs try to maximise individual sensor selectivity, the so called electronic nose approach combines many different non-selective sensors into an array of sensors and uses pattern analysis to discriminate between multiple gases, creating a so called electronic nose. Combining a large amount of sensors forces the reduction of individual sensor dimensions in the array in order to limit the overall size of the electronic nose and its energy consumption. This motivates the development of multiresponse sensor materials where a single unit of sensing material outputs multiple response signals.

The vast majority of metal oxide gas sensors use electrical conductance (EC) as the response signal of the sensor. A relatively little studied approach in the field of metal oxide gas sensors is to use photoluminescence (PL) intensity or decay rate as a response signal alternative to EC. It opens up opportunities such as remote contactless sensing, new material morphologies and dual sensing combining EC and PL.

1.2. Overview of the thesis

I focussed on the optical oxygen sensing using anatase phase TiO_2 nanopowder material doped with a small amount of Sm^{3+} ions (denoted as TiO_2:Sm^{3+}). The optical response signal investigated was Sm^{3+} impurity induced PL intensity and PL decay rate. Oxygen is an excellent sample gas since it is inexpensive, relatively safe and acts as a good sensitivity indicator – in case of metal oxide gas sensors, sensitivity to oxygen often indicates sensitivity to other gases as well. Since prior to this work very little was done in the field of lanthanide doped metal oxide based PL gas sensing, the first part of this thesis concentrates

on general characterisation of the material and its oxygen sensing capabilities. It continues with a more detailed analysis of the PL and its dependence on oxygen gas by quantitatively analysing the decay profiles of PL. Finally, the results of the quantitative analysis are used to point out potential causes of PL oxygen dependence.

The second part of this thesis unifies the more traditional EC based sensing with the PL based sensing creating a dual response sensor where a single unit of sensing material outputs two sensor signals simultaneously. The dual response sensor is subjected to a long experiment cycle where oxygen content is varied pseudo-randomly, simulating a real life usage scenario. The recorded dual signal of this cycle is then used to calibrate the sensor and I will show that using the two signals simultaneously increases the precision of the sensor two times.

1.3. Aims of the thesis

The general goal of this thesis was to obtain a detailed understanding of the gas sensing properties and capabilities of the TiO_2:Sm^{3+} material. The more detailed objectives were:

- To characterise the structure, phase and morphology of the TiO_2:Sm^{3+} material; to characterise the optical properties of the material; to properly characterise the material as an oxygen sensor.
- To create a qualitative and a quantitative model that describes the processes related to Sm^{3+} induced PL in the material and to use the model to identify probable mechanisms through which ambient oxygen content influences the intensity and decay rate of PL.
- To build a sensor where both PL intensity and EC of a single sensor material element can be simultaneously monitored; to design an oxygen cycle and a mathematical approach that can be used to assess the performance of the two sensor signals both separately and combined.

In this thesis it will be shown that:

- The properties TiO_2:Sm^{3+} PL are dependent on the oxygen concentration of its gas environment.
- Oxygen causes the increase of TiO_2:Sm^{3+} PL intensity.
- The change of PL intensity is caused mainly by a change of PL quenching centre concentration.
- The material can operate in a dual sensing mode, where oxygen is measured simultaneously by optical and electrical response signals.
- The dual sensing can be utilised to increase the precision the the sensor material.

2. BACKGROUND

2.1. Quenching based optical oxygen probes

The present work deals with optical oxygen sensing using photoluminescent inorganic semiconductor materials. However, the most common type of PL based oxygen sensors is instead based on organic molecules. In these sensors oxygen acts as a collisional PL quencher [1]. Collisional quenching takes place when oxygen comes to a contact with an excited PL emitter and the excitation energy is transmitted to the oxygen molecule via resonant energy transfer (RET) [2]. Fig. 1 illustrates the involved processes.

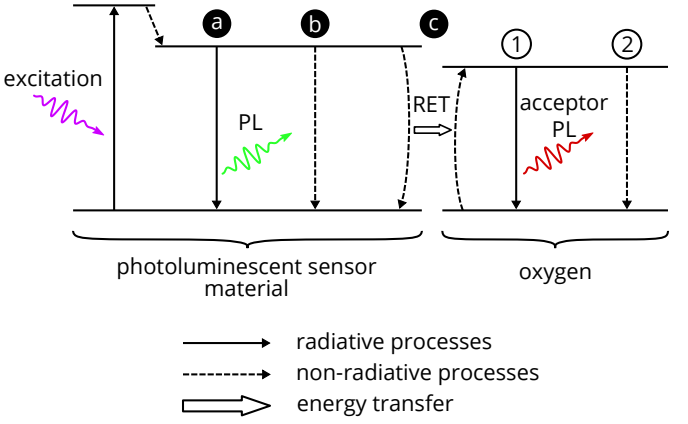

Fig. 1. The working mechanism of a PL quenching based oxygen sensor. There are three competing processes that can take place after the sensor molecule has been excited: a) photoluminescence, b) thermal relaxation and c) energy transfer to an oxygen molecule (if one is present). The excited oxygen molecule can either 1) emit a PL photon or 2) relax thermally.

The response of quenching sensors usually follows the Stern-Volmer law:

$$\frac{F_0}{F} = 1 + K_{\mathrm{D}}[\mathrm{O}_2] \tag{1}$$

where F_0 and F are the unquenched and quenched PL intensities and K_{D} is the Stern-Volmer constant. There are, of course, deviations from this very simple formula, but as a first approximation the quenching sensors can be characterised by a very limited set of parameters.

There is a rather wide array of various quenching sensor materials available. Most of the materials can be divided into two classes: organic probes and metal-ligand complexes [3]. The first organic probe material was discovered in 1939 [4], it is a polycyclic aromatic hydrocarbon (PAH). The PAH subclass contains

various other organic probe materials as well with much improved parameters compared to the original material [3]. Another subclass of the organic probe materials is fullerenes. This subclass contains some of the most sensitive oxygen sensors [5]. The second class of quenching sensors, the metal-ligand complexes, is mostly made up of ruthenium, iridium, osmium and rhenium complexes and large variety of (metallo)porphyrins [3].

It should be noted that the optical quenching based class of oxygen sensors is rather well studied and as of 2015 there were several companies that manufactured these sensors on a commercial scale [1].

2.2. Semiconductor metal oxide gas sensors

The previous section provided a very general background of PL based gas sensing. Next I will introduce the class of sensors where TiO_2 actually belongs to – the metal oxide based semiconductor gas sensors. It is probably the most widely used and studied class of gas sensor materials. Their popularity is based on their performance: they are sensitive, stable, can operate at high temperatures and have short response times. At the same time they are easy and cheap to manufacture and to maintain [6].

Gas sensing is based on the adsorption of gas molecules onto the surface of the metal oxide material. The most typical surface adsorbate is oxygen, as in a common application a sensor measures the concentration of some gas of interest (a toxic or explosive gas, for example) in air and therefore oxygen is always present. The exact form of surface oxygen species is dependent on temperature [7]. Nevertheless, numerous studies have detected the presence of various surface oxygen species such as O_2, O_2^- and O^- using methods such as electron spin resonance [8–10] and temperature programmed desorption [11, 12].

The surface oxygen species attract an electron causing the appearance of a charge depletion zone under the surface of the material. As a result, the electrical conductance of the material changes. Depending on the morphology of the material this can be caused by two mechanisms. Firstly, if the material consists of a thin film or small grains, then most of the material is within the charge depletion zone and the conductance changes due to the depletion of free charge carriers. Secondly, the depletion zone creates potential barriers between the material grains that also affect the conductance. For this reason, either nanopowders or thin films are used for sensing [7, 13].

Additionally, reducing gases may react with the surface oxygen adsorbates thereby affecting the surface oxygen concentration. This mechanism allows the semiconductor gas sensors to detect both oxidising and reducing gases [13].

The surface mechanisms described above apply when the operating temperature of the sensor is relatively low – typically 200 °C – 500 °C [6]. At higher temperatures (above approx. 500 °C) bulk processes start to play a significant role in sensor response mechanics [6]. This is the basis of the solid

electrolyte type gas sensors that are widely employed in the automotive industry [14, 15].

Empirically, the response of semiconductor gas sensors typically follows a power law:

$$S = A \cdot C^{\alpha} \tag{2}$$

where S is the response signal of the sensor (electrical conductance), C is the concentration of the gas being measured and A and α are empirically determined constants. A number of various response models have been observed [16] and a quantitative theory also exists that justifies the power law behaviour [17].

A rather wide array of different metal oxide semiconductor materials exists that have been used as gas sensor materials [6, 18, 19]. Probably the best known and most studied [18] is SnO_2 [20, 21]. Other most common materials include ZnO – studied in one of the first works regarding metal oxide gas sensors [22] and numerous later ones [23–27], TiO_2 [28–30] and WO_3 [30–34]. Composite oxides are also a possibility [30].

The number of gases detectable by the semiconductor metal oxide gas sensors is also very large [6, 19]. As a consequence, the semiconductor gas sensors are not very selective.

2.3. Multiresponse gas sensing

A traditional ideal gas sensor has a response to only one target gas and it does not react to other gases in any other way. Real sensors are usually not ideal and therefore have some kind of a response to various other gases as well. In a world that is full of various gaseous chemical compounds either case is not very practical – the perfect sensor can only sense a single gas and a universal gas sensor would therefore require an array of sensors, one sensor for each gas of interest. The number of "interesting" gases can be very large. The non-ideal gas sensor has always some interferences present.

A solution to the aforementioned problems is the so-called electronic nose. The original motivation behind the e-nose was to mimic the mammalian nose [35]. The idea behind the e-nose is to combine multiple non-selective but different sensors into a single device and use pattern analysis on the response signals to discriminate different gases. In such a way the e-nose (and the mammalian nose) can, with a relatively limited selection of sensors, detect a very large amount of gases. As a bonus we do not have to worry about the low selectivity of individual sensors.

The main applications [36] of electronic noses are food quality assessment [37], environmental monitoring [38, 39] and health assessment [40–42].

Many modern electronic nose setups align the individual sensors into a monolithic array as opposed to discrete, individual sensors [43, 44]. The number of sensors in an e-nose setup can become very large [45]. This means that the

sensor signal processing becomes a complex machine learning problem. It is notable that an overview of e-nose signal processing methods [46] covers a large portion of well-known machine learning techniques. The design of a proper e-nose therefore requires a proper understanding of not only the physics and material science of the physical sensors, but also the mathematical and statistical aspects of signal processing. Poor understanding of the signal processing techniques can lead to serious data misinterpretation [47].

The reason why I introduced the electronic nose is that later in this work I will introduce results demonstrating how two different sensor response signals – optical (PL intensity) and resistive – can be extracted from a single unit of gas sensitive material and how the two signals can be utilised. It has been suggested that such multivariate sensor materials are a next step in gas sensor and electronic nose development [48]. Examples of such multivariate behaviour include, for instance: capacitance and conductance of carbon nanowires [49], mass and current of a graphene FET [50] and various electrical parameters of a Si nanowire FET [51]. Optical signals, such as absorbance [52] and shift of reflectance [53] can also be combined with electrical signals. PL has been integrated into a mass sensor [54]. The combination that I used in the present work – PL and a resistive signal – is relatively rare. Most examples are based on porous silicon [55–57] and ZnO [24, 58, 59]. I would point out that, unlike the present work, most of the works combining PL and resistive responses do not attempt to extract any useful value out of the combination of the two signals.

2.4. Properties of TiO_2

Since the present work is wholly based on TiO_2, let's take a brief look at its properties and uses.

TiO_2 is a wide-bandgap semiconductor metal oxide material with 3 common crystallographic phases: anatase, rutile and brookite, with anatase and rutile being the most common phases. The bandgap of anatase is about 3.2 eV [60–62] and rutile is 3.0 eV [63–65]. Both rutile and anatase are optically anisotropic, with refactive index roughly between 2.5 and 2.9 [66]. Oxygen vacancies commonly present in the material give TiO_2 n-type conductivity [66]. Notice that the bandgap – corresponding to roughly 390 nm – lies just above the visible spectrum of light, meaning that for the naked eye the TiO_2 is colourless. As-prepared sol-gel TiO_2 is generally amorphous, mild heating causes the formation of anatase crystallites. At temperatures above 500-800 °C the rutile phase gradually appears [67–69]. Chemically TiO_2 is relatively inert [70]. Note that in case of a gas sensor the aforementioned properties can give the material an advantage as it can be integrated into processes involving a harsh chemical environment and high temperatures. The quenching based organic materials introduced in 0 are much more sensitive to temperature as the complex organic molecules tend to degrade at higher temperatures.

By volume, the largest application of TiO_2 is white pigment, mostly in paints, plastics and paper [70]. Its relatively large bandgap ensues its white colour and the high refractive index gives the pigment high opacity [66]. Another common use of TiO_2 is in sunscreens – the 390 nm bandgap means that it is transparent in the whole visible range but absorbs most of the UV [66]. TiO_2 is also commercially used as the sensing body of gas sensor materials, as was discussed above, and in photoassisted self-cleaning surfaces [71].

Proposed applications of TiO_2 are photocatalytic water purification and photocatalytic water splitting for H_2 production [71]. Both of these have had limited commercial success, despite extensive academic studies.

2.5. Photoluminescence of lanthanide ions in TiO_2

TiO_2 as a semiconductor material is itself photoluminescent [60]. However, it is possible to modify the PL spectrum and the underlying PL mechanism with the addition of impurities.

In the context of the present work we are mostly interested in lanthanide ion induced PL. A characteristic property of the lanthanide ions is that their 4f electron orbitals are shielded by the filled $5s^2 5p^6$ orbitals. It means that the energy levels of the 4f orbitals and optical transitions between them are relatively unaffected by the surroundings of the lanthanide ion, giving each lanthanide ion a characteristic PL spectrum. The shielding also ensures that the 4f-4f transitions have a narrow spectral range, as the reorganisation of electrons within the 4f orbitals have little effect on the binding pattern of the lanthanide ion. Quantum mechanical theory states that the 4f-4f transitions are forbidden, which in reality means that their probability of occurrence is low. Consequently, direct excitation of lanthanide ions is difficult, but once excited the lanthanide emission has a long lifetime, that allows lifetime measurements with relatively slow and inexpensive detectors [72].

A way to overcome the problem of inefficient excitation is to incorporate the lathanide ions into a host material that absorbs the excitation wavelengths efficiently and then transfers the excitation non-radiatively to the lanthanide ion. One of the original works utilising this idea used organic molecules as the host material [73], however inorganic semiconductor materials, such as TiO_2 are suitable as well [74–76]. A rather wide array of lanthanide ions have been shown to be luminescent in a TiO_2 host: Nd, Yb, Er, Tm in IR, Eu, Sm in red and Ho, Er in the green part of the spectrum [75, 76].

Fig. 2 summarises the PL related processes in a lanthanide doped semi-conductor material. An exciting photon excites an electron from the valence band into the conduction band. The excited electron then probably thermalises to some kind of an intermediate state whose exact nature is difficult to determine. Then, the electron can relax to ground state by emitting a PL photon or it can non-radiatively transfer its energy to the lanthanide ion, causing a 4f

electron to excite to a higher 4f level. Finally, the lanthanide ion emits a PL photon. Thermal relaxations (not shown in Fig. 2) can take place as well [76, 77].

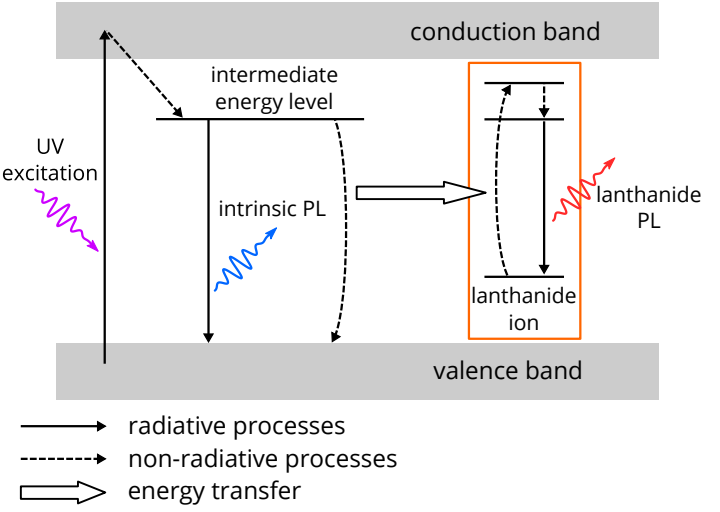

Fig. 2. Energy diagram and processes leading to PL in a lanthanide doped semiconductor.

2.6. Photoluminescence based gas sensing using metal oxides

At this point I am ready to combine all the topics introduced in this chapter and introduce the TiO_2 based optical gas sensor material. While ordinary semiconductor gas sensors use EC as the response signal it turns out that EC can be replaced by PL. Examples include all the common metal oxide sensor materials such as SnO_2 [78–80], ZnO [24, 80–86], TiO_2 [80, 87, 88], WO_3 [80] and In_2O_3 [89]. In all these cases intrinsic PL was used – it was emitted by the main sensor material itself and not by a dopant element.

In the present work we used the PL strategy outlined in section 2.5, so that PL was emitted by dopant lanthanide ions. This puts some limitations on the material. The band gap cannot be neither too large (difficult to excite) nor too narrow (the photoelectron cannot excite the dopant ion). Phase temperature stability is also an issue as abrupt phase changes during heating can damage the material so that the lanthanide dopant ions no longer emit PL. Heating to at least 500 °C is a necessary step of the sol-gel material preparation process.

Consequently, there are not too many previous works where dopant induced PL is utilised as a sensor response signal. Earlier examples include a Eu_2O_3-γAl_2O_3 [90], TiO_2:Sm^{3+} [91] (a spiritual predecessor of my work) and TiO_2:Eu^{3+} [92]. Later examples published during my PhD studies include TiO_2:Eu^{3+} [93], $Sr_4Al_{14}O_{25}$:Eu^{3+}/Dy^{3+} [94], $(K_{0.5}Na_{0.5})NbO_3$:Pr^{3+} [95], TiO_2:Sm^{3+}/metal-organic framework [96] and ZrO_2:Eu^{3+},Nb^{5+} [97].

3. EXPERIMENTAL

The gas response measurements formed a central part of this work. They were performed using a custom made experiment setup. The principal elements of this setup are depicted in Fig 3. The setup is built around a sample holder cell (Linkam THMS350V) equipped with connections for gas flow through, temperature control, a window for optical measurements and electrical connections for conductivity measurements. The sample is illuminated by a pulsed 355 nm laser (Elforlight) or a continuous 365 nm UV diode (Thorlabs). The laser was run at 5 kHz for PL intensity measurements but at 200 Hz for PL decay measurements. PL spectra were registered with a CCD (Andor DU240-BU), decays with a PMT (Hamamatsu R2949) coupled with a photon counting multiscaler (Fast ComTec P7888). Electrical conductance was recorded with a precision source measurement unit (Keithley K2400 or K2450) at constant 1 V voltage. The gas composition of the interior of the sample cell was manipulated by feeding a mixture of oxygen and nitrogen continuously through the sample chamber at 200 ml/min. The source gases were oxygen, nitrogen and a mixture of the two with 10% oxygen and 90% nitrogen; all gases were 99.999% pure. Gas flow rate and composition were regulated by mass flow controllers (Brooks SLA 5850 or Bronkhorst EL-FLOW).

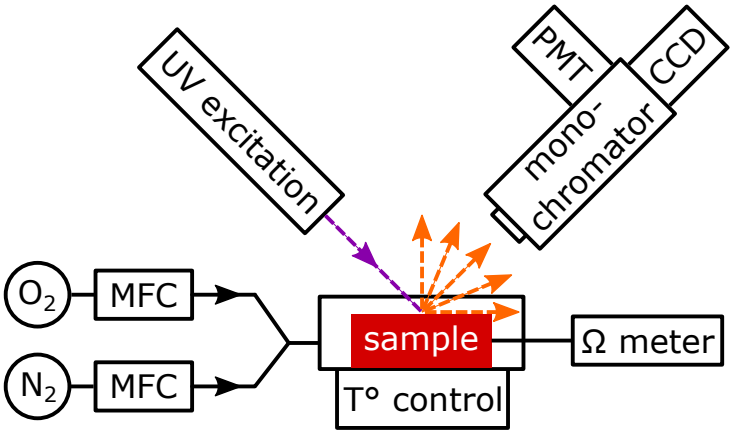

Fig. 3. A diagram of the gas response experiment setup.

4. SAMPLE PREPARATION AND CHARACTERISATION

4.1. TiO_2:Sm^{3+} material preparation

The very first step of the experiments was to prepare well defined samples that can be studied in following gas sensing experiments. The material that we chose to study was TiO_2 doped with Sm^{3+} ions in a nanopowder form. We made the samples in two steps. First, a TiO_2:Sm^{3+} nanopowder was prepared using the sol-gel method. The nanopowder was annealed at 800 °C. As the result of the first step we got a material that was in principle capable of gas sensing. In the next step we deposited the material onto quartz substrates (~10 × 10 × 1 mm). This was done by dispersing the powder obtained in the first step in distilled water using an ultrasound probe. A drop of the resulting TiO_2 emulsion was transferred onto the substrates. After the water had evaporated the TiO_2 formed a solid white layer. In the end we obtained durable samples that could be systematically tested in the gas sensing and other experiments. For purely optical experiments the sample substrate was pure quartz, for experiments that required measuring the electrical resistance of the sample material a special glass substrate (IME 2050.5 M-Au-U, ABTECH Scientific Inc., ~ 10 × 5 × 1 mm) with gold interdigitated electrodes was used (Fig. 4).

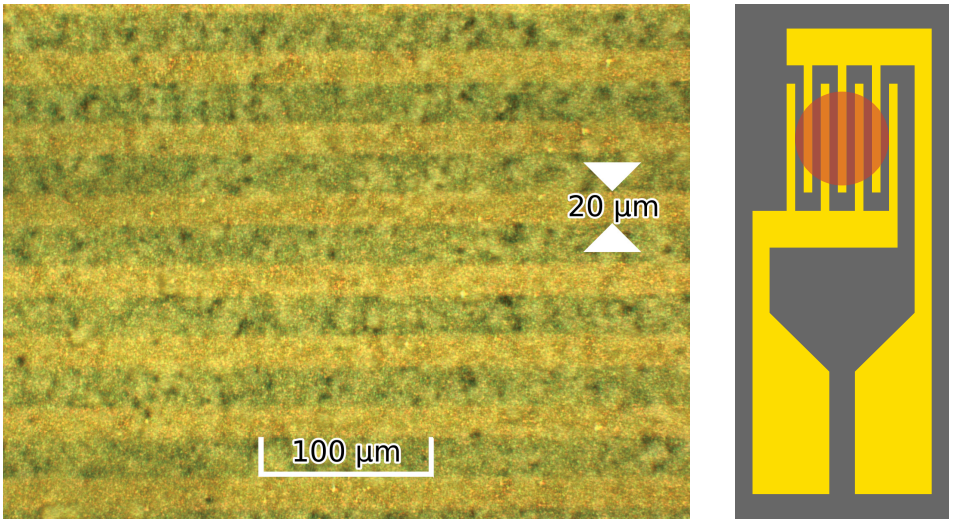

Fig. 4. Left: an optical microscope image of the sample powder on gold interdigitated electrodes. Right: a diagram of the sample substrate with gold electrodes. The red circle marks the approximate location of the sample powder.

4.2. Morphology

SEM micrographs (Fig. 5) taken of prepared samples give a visual overview of the structure of the nanopowder. Based on a visual interpretation of the SEM images the material consists of agglomerated nanocrystallites that form a porous layer with a somewhat hierarchical structure. The agglomerated nanocrystallites form structures with a diameter of several hundred nanometers. The crystallites themselves have a diameter of roughly 40 nm, based on a set of random measurements on the micrograph.

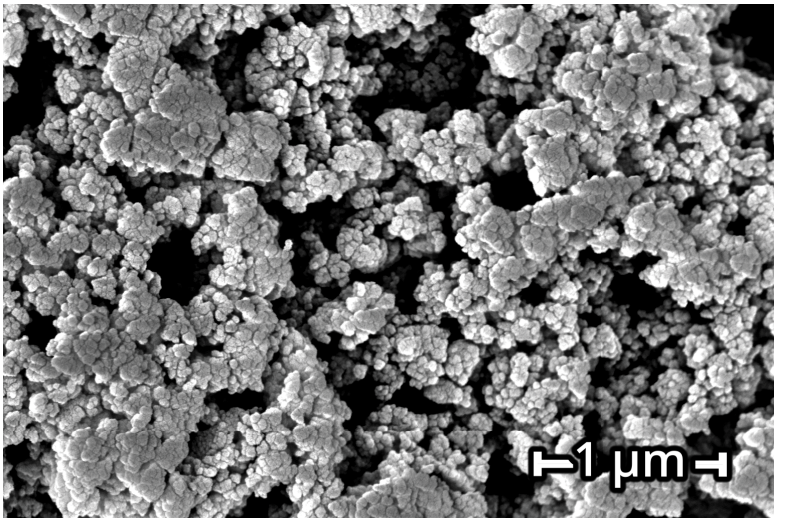

Fig. 5. SEM image of the prepared $TiO_2:Sm^{3+}$ sample.

A more quantitative way to describe the structure of the material is to measure its differential pore volume distribution using the BET method. The distribution (Fig. 6) indicates two maxima near 40 nm and 150 nm. This confirms the description determined from the SEM image.

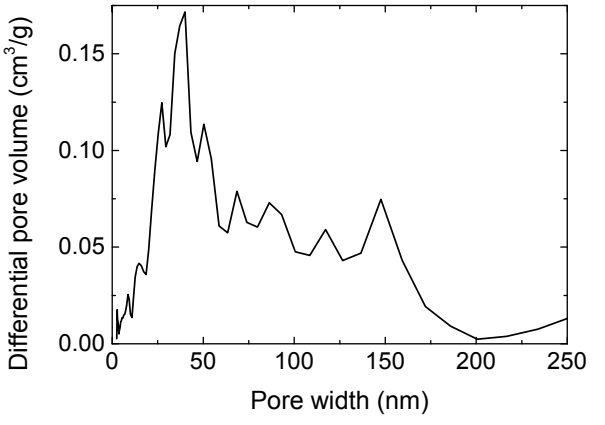

Fig. 6. The differential pore volume distribution of the TiO_2 material determined by the BET analysis.

An important aspect of a semiconductor material is its crystal phase. In case of TiO_2, the most common phases are rutile, anatase and brookite. One of the most simple methods to determine the crystal phase of TiO_2 is to measure its Raman spectrum. The Raman spectrum of the material (Fig. 7) reveals that the crystalline phase of the material is anatase and no indications of rutile or brookite. At grain sizes less than 20 nm the Raman peaks are known to broaden and shift [98]. These changes were not observed, which indicates that the crystallites are larger than 20 nm, in accordance with the estimations from the SEM images.

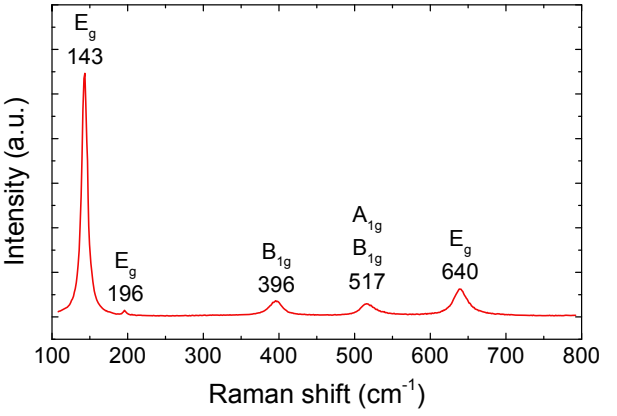

Fig. 7. The Raman spectrum of the prepared TiO_2:Sm^{3+} nanopowder. The spectrum is typical of anatase.

4.3. Optical properties

Since the goal of this work is to characterise the optical gas sensing capabilities of the TiO_2:Sm^{3+} material, lets first take a look at its optical properties. Namely we are interested in the emission and excitation spectra. To measure an emission spectrum, we need a light source. We used a 355 nm laser. This wavelength corresponds to a photon energy of 3.49 eV. The band gap for TiO_2 has been measured at 3.2 eV for anatase single crystals [60] and 3.2-3.3 eV for nanomaterials [61, 62], so our 355 nm excitation is well above the band gap of the material.

A typical emission spectrum of the TiO_2:Sm^{3+} nanopowder is presented in Fig 8. The spectrum consists of a wide emission band centred near 525 nm and four sharp bands near 583, 612, 662 and 725 nm. Such two component composition (eg. wide band + sharp peaks) is typical of the TiO_2:Sm^{3+} material and spectra with a similar character have been seen over a wide array of experiments with the material over the course of this work and also previously [99]. The wide band emission is believed to be intrinsic to anatase, coming either from self trapped excitons, bound excitons or defect sites [60, 99–102]. The sharp

transitions are caused by the radiative transition between the Sm^{3+} ion 4f shell energy levels, from the $^4G_{5/2}$ to ^6H_J levels (labelled accordingly in (Fig. 8) [103].

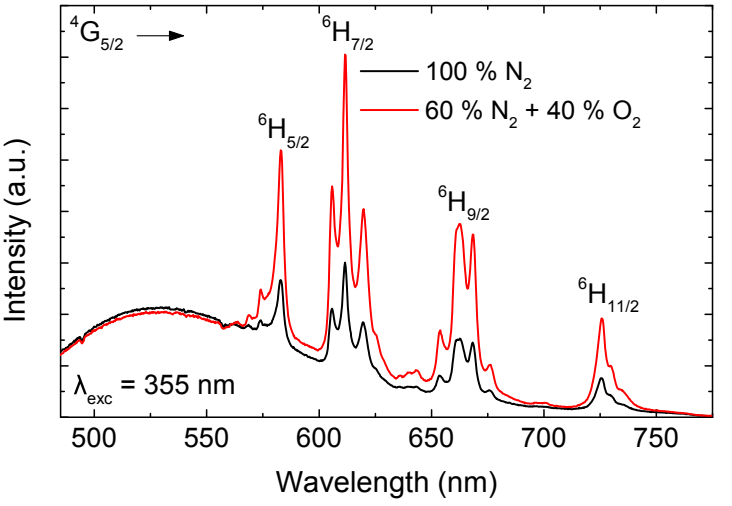

Fig 8. Typical emission spectra of the TiO_2:Sm^{3+} material excited with 355 nm. The spectra are given at two different ambient gas compositions to demonstrate how the relative proportions of the spectrum can vary.

The PL excitation spectrum shown in Fig. 9 was recorded at the most intense Sm^{3+} peak at 612 nm. It confirms that the 355 nm excitation is well in the region where the PL excites efficiently. The excitation spectrum can be used to estimate the band gap the material using the Tauc plot (Fig. 9 inset). The band gap determined by this method is 3.27 eV, similar to the band gap values (~3.2 eV) found in literature cited in section 2.4.

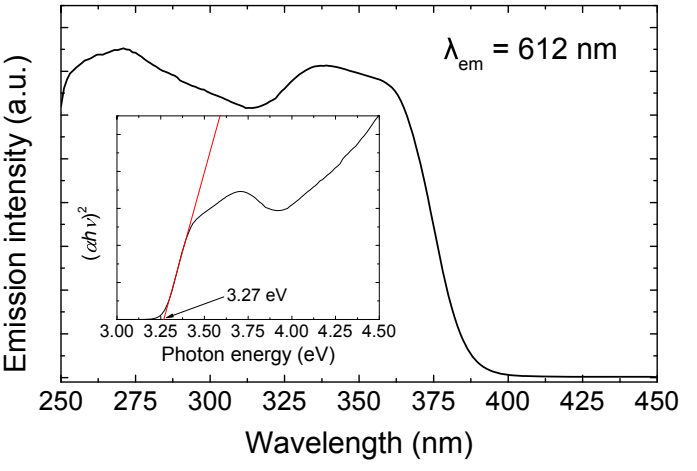

Fig 9. PL excitation spectrum of the TiO_2:Sm^{3+} material recorded at 612 nm. The inset shows the Tauc plot with the same data.

The two spectra exhibited in Fig. 8 give a general understanding of how the shape of the spectrum depends on ambient gas composition. Namely, the intensity of the wide band emission at 525 nm remains mostly the same and the intensity of the sharp Sm^{3+} lines changes. So our interest is mostly directed towards the intensity of the Sm^{3+} emission, which in simple terms means the area under the Sm^{3+} lines with the part of the 525 nm wide emission band subtracted to get rid of a near constant baseline. Our experiments have shown that the relative intensity of the Sm^{3+} lines do not change. Therefore, the intensity of the whole Sm^{3+} spectrum can be rather well estimated by only integrating the area under one of the peaks. This is illustrated in Fig 10. The yellow region in the figure depicts the area that is integrated to obtain a numeric value for PL intensity.

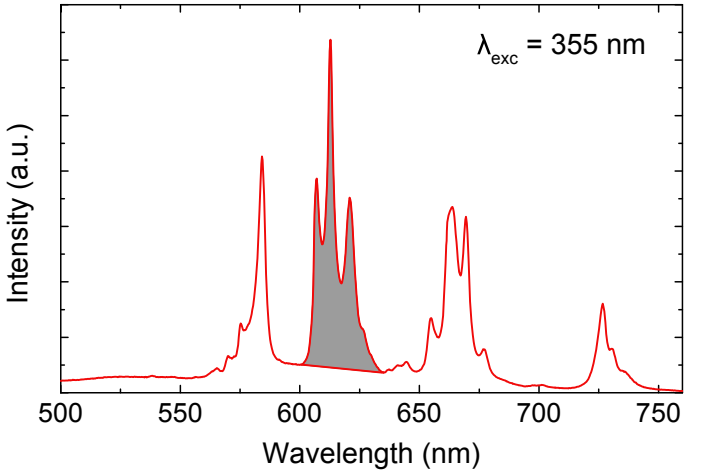

Fig. 10. The gray part under the TiO_2:Sm^{3+} emission spectrum represents the area that is integrated to obtain the numeric value for what is referred to as "PL intensity" in this work.

4.4. Electrical properties

TiO_2 is a well known semiconductor gas sensor material. Usually the measured response signal of the material is its electrical conductance (EC). Therefore, it is a logical step to see how our synthesised material behaves as a traditional electrical sensor. Considering that the goal of this work is to study the material as an optical gas sensor it would be interesting to simultaneously observe the behaviour of the PL intensity (PLI) (that I defined in the previous section) and EC. The simultaneous PLI + EC based gas sensing experiments are introduced in chapter 6. We must note however that when we measure both signals simultaneously, then the UV used to excite PL also has an effect on EC. Therefore, in this section I will investigate how UV irradiation affects the properties of the sensor material.

Fig 11 illustrates how PLI and EC change when the UV irradiation source is switched on and off. The presence of UV causes the EC to rise several orders of magnitude. It is also notable that the change in conductance takes several tens of seconds to stabilise. A traditional explanation of the photoconductivity is that it is directly caused by the conduction electrons induced by the optical excitation of valence electrons to the conduction band. However the situation is probably different in case of metal oxides because the extent and temporal dynamics of photoconductance depends on the surrounding gas atmosphere [104–106]. In case of a WO_3 sample it has even been observed that the change in photoconductance was permanent in vacuum but reversible in air [105]. It is also known that optical stimulation causes the release of surface oxygen [107, 108]. Therefore it is likely that the photoconductance is caused by photodesorption of surface oxygen species and the subsequent release of surface trapped charge carriers, as proposed in [104].

Considering the photoresponse behaviour depicted in Fig 11 and the argumentation above it becomes clear that as long as UV is applied the material operates in a mode where the conductance and surface reactions are heavily influenced by optical irradiation. This becomes particularly important later when I introduce gas sensitivity experiments where PLI and EC are recorded simultaneously. The situation is somewhat similar to several earlier works that studied the gas sensing properties of metal oxides under UV. The idea behind these works was to enhance sensitivity and reduce operating temperature in an otherwise ordinary EC based metal oxide gas sensor [109–111]. In our work, UV irradiation is a fundamental part of the sensor as it excites PL in our PL based sensor material.

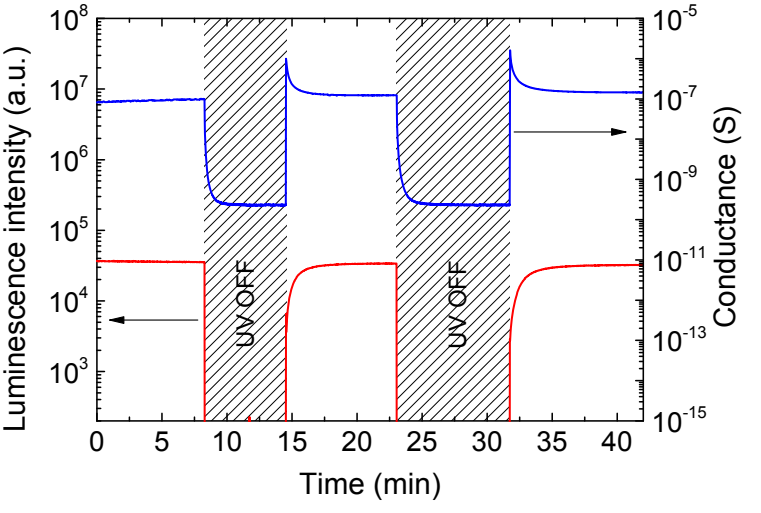

Fig. 11. The effect of 355 nm laser irradiation on the PL intensity and conductance of the material.

5. PHOTOLUMINESCENCE BASED OXYGEN SENSING (PUBLICATION I, II, III)

5.1. Photoluminescence dependence on oxygen content

In this chapter I will introduce the optical gas sensitivity experimental results that form the core of this thesis. A relatively simple yet insightful way to obtain an overview of the capabilities of a sensor is to monitor its response while introducing a sequence of gas concentrations to the experiment chamber. Fig. 12 presents the temporal response curve acquired in such an experiment. The TiO_2:Sm^{3+} sample was subjected to a series of 10 min oxygen cycles with decreasing oxygen concentration. Between the oxygen cycles pure nitrogen was fed to the test sample. We found that oxygen causes the PLI to increase while nitrogen has the opposite effect. The experiment was conducted at 25 °C which for a metal oxide gas sensor is a very low temperature. The temporal response experiment also indicates that the material is capable of sensing oxygen in a wide range of concentrations. It can detect oxygen starting from 100% down to < 0.01% (roughly equivalent to 100 ppm).

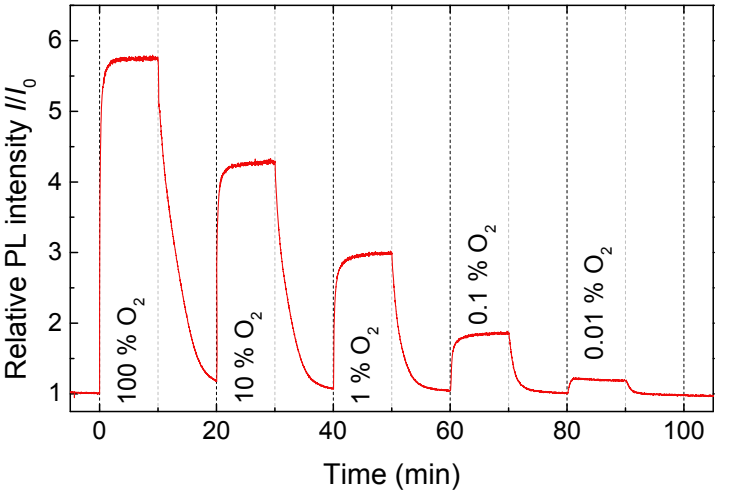

Fig. 12. The temporal PL signal response to a wide range of oxygen concentrations.

Typical recorded response times (the time it takes the signal to reach 90% of the final value) were about 1 min and recovery times about 5 min. However, this includes the response time of the measurement chamber (estimated about 20 s) and therefore the true response time can be somewhat faster.

Fig. 13 depicts the stationary response profile of the sensor material. In this plot the relative PL intensity values from Fig. 12 at the end of each oxygen cycle are plotted against oxygen concentration. It is assumed that the oxygen cycles are long enough for the PL intensity to reach a final value. The stationary

response profile resembles a power law (Eq. 1), where S is the PLI response of the sensor. The stationary response somewhat deviates from a pure power law, however, the deviation is not so significant if the range of oxygen concentations is decreased. A somewhat similar power law behaviour has been observed in EC based semiconductor gas sensor materials [17].

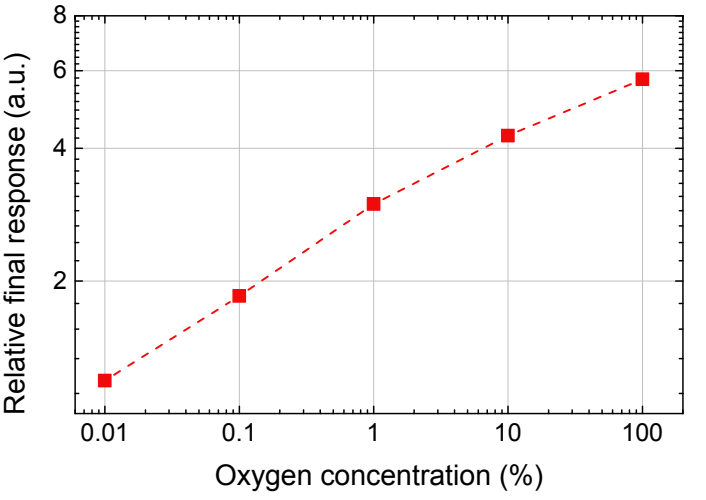

Fig. 13. The stationary response profile of the sensor material. In this plot the values of relative PL intensity at the end of each oxygen cycle (Fig. 12) are plotted against oxygen concentration, revealing a near power law response behaviour.

5.2. Proposed optical sensing mechanism

The EC based response mechanism has been widely studied and there is a general agreement as to what could be the reasons that cause EC to be dependent on ambient gas composition. On the other hand, little is known about the mechanism of PL gas sensitivity. To obtain a better understanding of this mechanism we recorded and analysed the PL decay curves, that provide much more information about the PL related processes in the material than the integral PLI. Another advantage of this method is that during the recording of the decays the sensor material operates in conditions that are very similar to the conditions during normal sensor operation.

The method I will introduce in this section can be summarised as follows: a series of decay curves are recorded over a range of ambient oxygen concentrations. Then a mathematical model (function) is fitted onto the experiment data. The mathematical models are based on physical processes that likely take place in the material. The models are elaborated until the quality of the fit becomes satisfactory. Finally, the parameters of the fitted models can be compared to pinpoint physical processes responsible for the changes of PL intensity and decay rate.

I showed in the previous chapter that the PL intensity decreases with oxygen content in the ambient gas. Therefore, it is natural to expect that the area under the decay curves also decreases with oxygen content. Mathematically there are generally two ways this could happen – either the initial value of the decay decreases and the whole decay curve is scaled down or the decay becomes faster.

A most simple decay can be characterised using an exponential function.

$$I(t) = I_0 e^{-\frac{t}{\tau_0}} + y_0 \tag{3}$$

Such decay would be observed, if the material contained a number of identical independent PL emitting centres. Upon excitation, each of the centres will emit a photon and return to the ground state within an average period of τ_0 or decay rate k_0.

$$k_0 = \frac{1}{\tau_0} \tag{4}$$

Ideally $y_0 = 0$, but usually background radiation causes $y_0 > 0$. If the number of PL emitters changes it is reflected by a change of I_0. If the decay becomes faster, then τ decreases.

The measured decays (Fig. 14) have a strongly non-exponential behaviour. This indicates that the decay process is more complicated than the simple model described above.

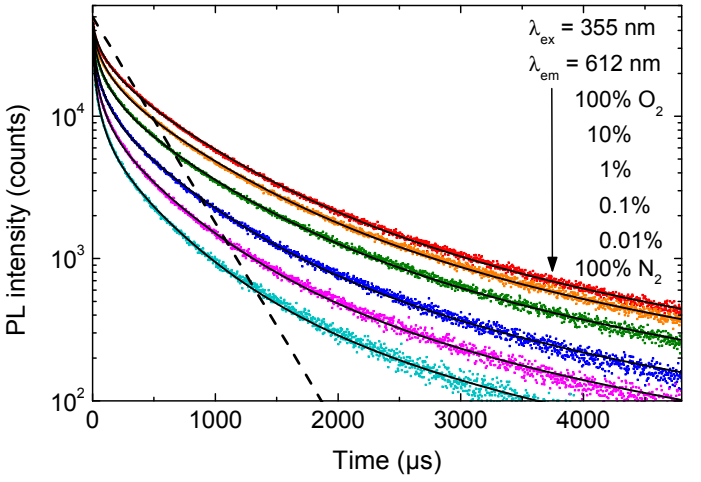

Fig. 14. The PL decay curves of the TiO_2:Sm^{3+} material registered at various oxygen concentrations.

A possible cause for a non-exponential decay is quenching. It means that some of the excited PL centres transfer their excitation energy to a quenching centre, which could be a lattice defect, impurity or even another PL centre. Quenching makes a decay faster. It can also cause non-exponential decay, because the quenching is not necessarily uniform for all PL emitting centres, leading to a distribution of the effective τ values of the PL centres. Another factor that can influence decay is delayed excitation. The exponential decay model assumes that at $t = 0$ all the centres are excited and afterwards only radiative relaxation processes take place. However, it is possible that some shallow traps absorb some of the excited electrons created in the semiconductor by the laser pulse. Thermal disturbances can cause the release of the trapped electrons some time after the start of the decay. These untrapped electrons can re-excite some of the PL centres. This delays the decay profile, opposed to the quenching effect. Either of the effects causes the decay profile to deviate from a pure exponential form.

To understand whether the non-exponential behaviour is caused by quenching, trap assisted delaying or both, it would be useful to know the natural decay rate of the PL centre – the Sm^{3+} ion – inside a TiO_2 host (denoted τ_0 in the following discussion). Measuring the natural decay rate is somewhat complicated as it requires the elimination of all sorts of influences that modify the raw behaviour of the ions. Several works have tried to achieve this and have obtained values 258–350 µs [67, 112, 113], so it is reasonable to assume $\tau_0 = 300$ µs. A purely exponential decay of 300 µs is depicted by the dashed line in Fig. 14. It appears that the initial part of the decays recorded in the experiment are faster and the end parts slower than the natural decay. This indicates that both quenching and delay is present in the material.

The argumentation so far outlines a qualitative explanation of the response of the decay curves to oxygen gas. I will now introduce a quantitative approach that helps us understand which effects have a role in the oxygen sensing process. To do so, I will outline a mathematical model based on physical laws that fits the registered decay curves. In this way it is possible to link the changes in the decays to physical processes as the free parameters in this kind of a model are no longer mere empirical constants but have a more real meaning.

Assuming we have an ensemble of identical PL centres surrounded by a random distribution of quenching centres the observed PL decay would take the form [114]:

$$I(t) = I_0 u(t) \tag{5}$$

$$u(t) = \exp\left(-k_0 t - \frac{c}{c_0}(k_0 t)^{\beta}\right) \tag{6}$$

k_0 is the natural decay rate of the PL centre. c/c_0 is a relative concentration of acceptors. Its exact connection with physical quantities is rather complex and contains further constants that have to be determined experimentally for a

particular material. However, as it is proportional to the concentration of quenching centres it will provide very useful information about the material. The power constant is defined as

$$\beta = \frac{D}{n} \tag{7}$$

where D is the Eucleidean dimensionality of the space and n depends on the type of interaction between the PL centre and the quenching centre, it is 6 for dipole-dipole and 8 for dipole-quadrupole interactions. In case of a uniform infinite 3D space $D = 3$, but in reality the conditions might not be perfectly met leading to a slightly lower D value.

Some number of PL centres that are excited at at some time point will decay according to Eq. 2 with the t parameter measuring time from the start of decay of these particular PL centres. However, since we have delayed excitation present, different PL centres start their decays at different times. Assuming we have a single type of traps present, the contribution from retrapping is negligible and that each untrapped electron instantly finds a PL centre to excite then the amount of trap assisted PL centre excitations follows

$$I_1 \exp(-kt) \tag{8}$$

where k is the rate of electron untrapping. So the number of PL centres that are excited via traps in the interval $t \ldots t + dt$ is

$$r(t)dt = I_1 k \exp(-kt)\, dt \tag{9}$$

Since these PL centres will start to decay according to $u(t)$ then the resulting observed decay would be the convolution between the two processes:

$$I_{\text{delayed}}(t) = I_1 \int_0^t r(t')\, u(t-t')dt =$$

$$I_1 \int_0^t k \exp(-kt') \exp\left(-k_0(t-t') - \frac{c}{c_0}\left(k_0(t-t')\right)^{\beta}\right) \tag{10}$$

Probably some of the PL centres are excited instantly, without the trapping and untrapping processes. These centres decay according to $u(t)$

$$I_{instant} = I_0 u(t) \tag{11}$$

The overall decay profile looks as follows:

$$I(t) = I_{instant} + I_{delayed} = I_0 u(t) + I_1 \int_0^t k \exp(-kt')\, u(t-t')dt \tag{12}$$

This function can be fitted onto the experimentally recorded decay profiles. The results of the fitting are illustrated by Fig 15. It turns out that the model described by Eq. 3 is not sophisticated enough to properly fit the experimental data. While the initial part of the decay is fitted adequately, the tail part of the model and experiment diverge significantly. This indicates that the trap electron release rate k is not constant but follows a distribution. Therefore Eq. 3 is further generalised:

$$I(t) = I_0 u(t) + I_1 \int_0^\infty dk\rho(k) \int_0^t k \exp(-kt')\, u(t-t')dt \tag{13}$$

where $\rho(k)$ is the distribution of the distribution of the electron untrapping rate. In order to fit the generalised model to the experiment data $\rho(k)$ has to be given a concrete form.

We assume that the trap depths have an exponential distribution [115]. The trap depth is the energy needed to untrap the photoexcited charge carrier. The exponential distribution of the depths is given by:

$$\rho_{\mathrm{E}}(E) = \frac{1}{\Delta E} \exp\left(-\frac{E}{\Delta E}\right) \tag{14}$$

where ΔE characterises the spread of the distribution. Assuming thermal release of carriers from the traps the Arrhenius equation provides a basic relationship between detrapping rate and trap depth:

$$k = k_{\mathrm{M}} \exp\left(-\frac{E}{k_{\mathrm{b}} T}\right) \tag{15}$$

where T is temperature, k_b is the Boltzmann constant and k_M is an attempt-to-escape frequency.

Our model requires the distribution function of the k parameter, so we need to perform a change of variables. According to the rules of distribution function variable change:

$$\rho_{\mathrm{k}}(k) = \left|\frac{d}{dk}E(k)\right| \rho_{\mathrm{E}}\big(E(k)\big) \tag{16}$$

where $E(k)$ is the inverse of Eq. 5 with respect to E. This assumes that both E and k are unbounded, but for simplicity's sake we can make this assumption. After necessary substitutions and simplifications:

$$\rho_{\mathrm{k}}(k) = \frac{R}{k}\left(\frac{k}{k_{\mathrm{M}}}\right)^{R} \quad R = \frac{k_{\mathrm{B}}T}{\Delta E} \tag{17}$$

This gives Eq. 4 a concrete form that can be fitted to the experiment data. The model with the trap depth distribution fits the experiment data adequately, as illustrated by Fig. 15. This is an indicator that the model adequately describes the physical processes that occur in the material.

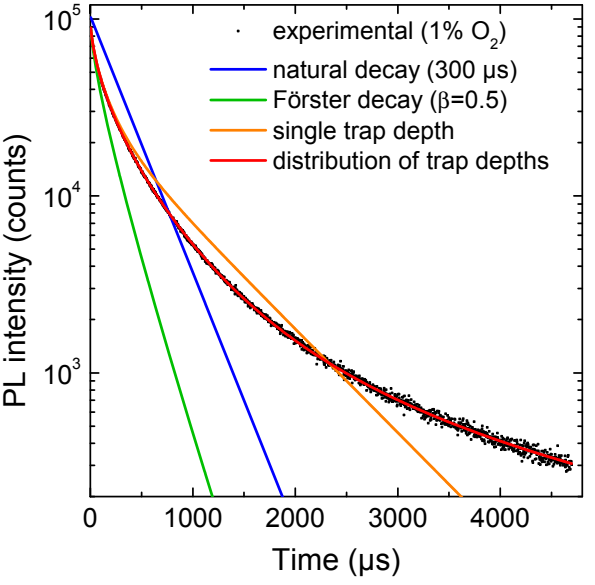

Fig. 15. An experimental decay curve (black dots) and various fitted models illustrating the need for a complex model with quenching and delayed excitation present.

Eq. 4 together with Eq. 6 forms a model that is defined by the following parameters: β, τ_0, R, k_m, I_0, I_1 and c/c_0. Out of these, τ_0 was fixed at 300 µs, according to the discussion and citations provided above. If the Sm^{3+} concentration remained low enough then the parameter β could be fixed at 0.5, which corresponds to an infinite 3D atomic lattice where the Sm^{3+} ions do not interact with each other. A more detailed discussion regarding the value of β is available in publication III. The rest of the parameters were fitted to the

experiment data. Table 1 lists the relative values of the fitted non-fixed parameters of the model. The relative values V_r are defined as

$$V_r = \left| \log_{10} \left(\frac{V}{V_{100\%}} \right) \right| \tag{18}$$

where V is the true value of the parameter and $V_{100\%}$ is the value of the parameter when oxygen concentration was 100 %. I omitted the true values V from this work since they carry little useful information in this context. However, we are very much interested which parameters change as a result of oxygen concentration change and for that purpose the V_r values are very useful.

Table 1. The relative values of parameters obtained by fitting the decay model to the experiment data.

	Sample 1					
	100 %	10 %	1 %	0.1 %	0.01 %	0 %
I_0	0	0.00	0.02	0.05	0.06	0.08
I_1	0	0.06	0.11	0.14	0.17	0.21
R	0	0.09	0.19	0.28	0.35	0.43
k_m	0	0.04	0.09	0.16	0.24	0.33
c/c_0	0	0.28	0.51	0.70	0.86	0.98

	Sample 1 several months later					
	100 %	10 %	1 %	0.1 %	0.01 %	0 %
I_0	0	0.01	0.00	0.01	0.03	0.02
I_1	0	0.03	0.10	0.16	0.22	0.26
R	0	0.03	0.10	0.15	0.18	0.20
k_m	0	0.02	0.06	0.16	0.25	0.28
c/c_0	0	0.09	0.17	0.29	0.40	0.43

	Sample 2					
	100 %	10 %	1 %	0.1 %	0.01 %	0 %
I_0	0	0.00	0.01	0.02	0.03	0.04
I_1	0	0.01	0.06	0.13	0.17	0.18
R	0	0.02	0.07	0.14	0.17	0.18
k_m	0	0.02	0.06	0.11	0.18	0.24
c/c_0	0	0.08	0.17	0.28	0.37	0.43

It turns out that out of the non-fixed model parameters, c/c_0 changes the most. It is further illustrated by Fig. 16. This parameter is proportional to the concentration of quenching centres inside the material. Therefore, we propose that

the change of quenching centre concentration is the main factor that modulates the decay rate and consequently the PL intensity.

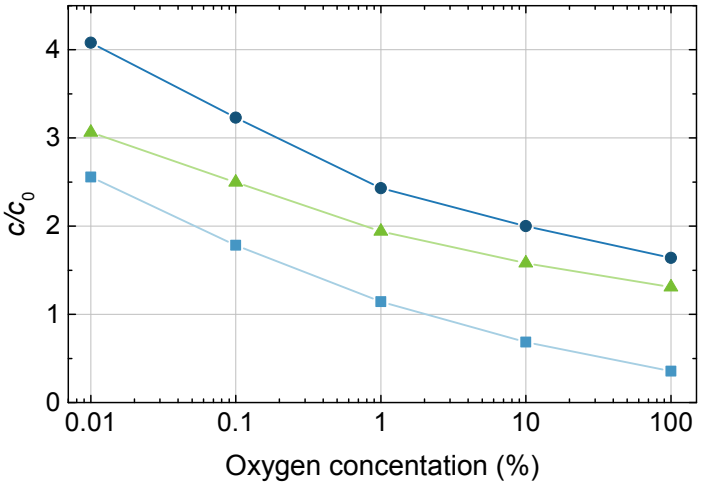

Fig. 16. The dependence of the model parameter c/c_0 on oxygen concentation. The different lines represent various experiments done with the same material.

The question remains how ambient oxygen concentration influences the amount of quenching centres. It is generally understood that at room temperature oxygen forms O_2^- radicals on the surface of TiO_2 [10, 116, 117] and the concentration of these surface radicals increases with increasing oxygen partial pressure. Since the oxygen radicals capture an electron from the TiO_2 material the radicals lead to a reduction of charge carrier concentration in the material, particularly near the surface [17]. Based on this we conclude that this carrier depletion causes the quenching centres to be effectively turned off. Being in an off state means that the quenching centre is not capable of (non-radiatively) receiving the excitation energy from the excited Sm^{3+} ion. Assuming that the quenching defect is a deep trap, then its deactivation can be achieved by removal of electrons from the trap. In this way the trap becomes unable to absorb energy. The deep trap can be an oxygen vacancy or a titanium interstitial [118].

Fig 17 summarises the processes involved with Sm^{3+} PL and its oxygen sensitivity.

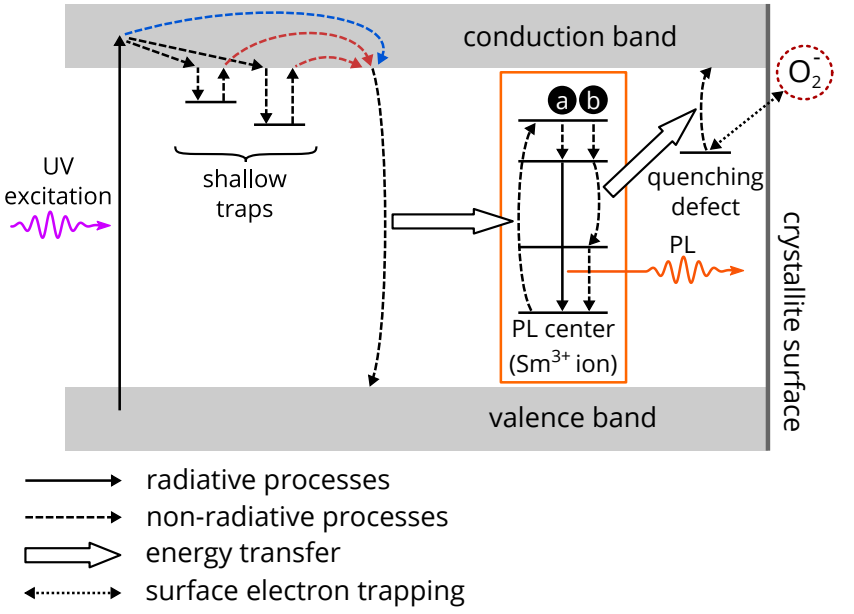

Fig. 17. A diagram illustrating the processes inside the TiO_2 material that lead to PL and its modulation by the ambient oxygen atmosphere. The material is excited by UV and the excitation energy is transferred to the Sm^{3+} ion either directly or in a delayed manner. The Sm^{3+} ion, once excited, can (a) emit a photon or (b) be quenched. The quenching defect can be turned on and off via electron transfer from the defect to surface oxygen radicals.

5.3. Oxygen sensitivity enhancement with Au/SiO_2 nanoparticles

In this short section I will give an example of how it is possible to improve the gas sensing capabilities of the TiO_2 nanopowder by incorporating it into a nanocomposite material.

The nanocomposite that we tested was a mixture of gold nanospheres with silica cores and sol-gel $TiO_2:Sm^{3+}$. The silica cores were about 200 nm in diameter, covered with much smaller gold nanoislands, leaving the silica core partially exposed. The $TiO_2:Sm^{3+}$ nanomaterial was prepared using the sol-gel method, the gold nanospheres were introduced to the precursor solution of the sol-gel process. For comparison, normal $TiO_2:Sm^{3+}$ was also prepared with exactly the same process, only without the gold nanospheres in the precursor. The material was spin coated on glass substrates and annealed at 500 °C.

The response of composite and normal samples to oxygen was recorded (Fig 18). We found that the sensitivity was over 4 times greater for the composite material.

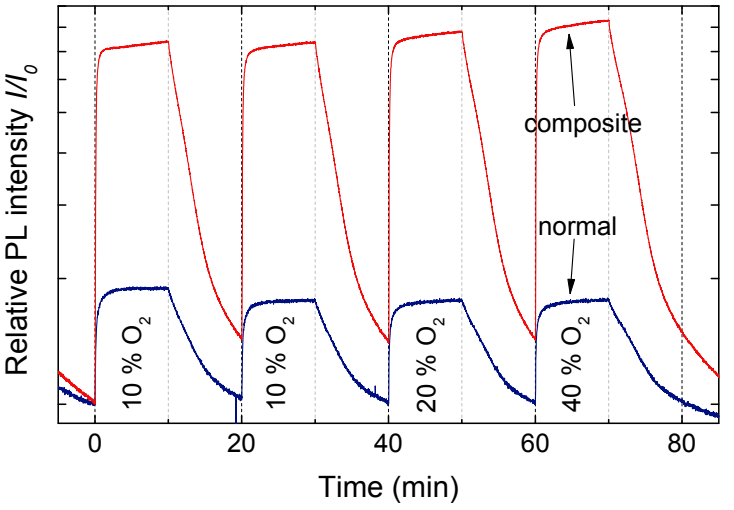

Fig. 18. The effect of Au/SiO_2 on the temporal PL signal response to oxygen.

To further understand the mechanics behind the enhancement, we performed a decay curve analysis for both the composite and normal samples. The decay measurement experiment and analysis was identical to what was used in the previous section, resulting once again in a table of model fitting parameters. Comparison of the fitting parameters indicated, in agreement with the previous results, that the c/c_0 parameter had the largest amplitude of change. However, the difference as well as the value itself was larger for the composite sensor material. We concluded that the introduction of the gold/silica spheres caused the concentration of the surface oxygen switchable quenching centres to increase, leading to improved gas sensitivity.

These results provide an example of how the basic material can be modified in order to enhance its sensing capabilities and how the decay based analysis can be applied to understand the mechanics of the enhancement. The fact that the decay analysis gave consistent results with the previous experiments somewhat validates the model introduced in the previous section. The options to design a nanocomposite are essentially unlimited, but there are also numerous other parameters that can be tuned when designing the optimal sensor material, such as dopant concentration, annealing conditions, material thickness, excitation wavelength, intensity etc.

5.4. Conclusions

The TiO_2:Sm^{3+} material has good PL based oxygen gas sensing capabilities. Both PL intensity and PL decay rate depend on ambient oxygen content. The material is capable of sensing oxygen in a wide concentration range starting at < 0.01 % up to 100 % at atmospheric pressure. Quantitative modelling of the

decay profiles reveal that the material PL decay is a complex process influenced by both excitation energy trapping and PL quenching. PL dependence on oxygen concentration is caused by quenching centre concentration modulation by oxygen. The oxygen sensitivity of the material can be enhanced by increasing the quenching concentration by mixing the TiO_2 based sensor material into a nanocomposite.

6. DUAL RESPONSE GAS SENSING (PUBLICATION IV)

6.1. Simultaneous resistive and PL-based sensing of oxygen

Much of this work concentrates on the optical gas sensing capabilities of TiO_2. On the other hand, as I explained in chapters 2.2. and 2.4, it is a well known electrical sensor material, where the response signal is electrical conductance (EC). Based on this knowledge I made experiments where the EC and PLI signals were recorded simultaneously. It turns out that the material is well capable of outputting the two response signals simultaneously, as illustrated in Fig 18, giving the sensor so called dual response capabilities. EC has similar oxygen dependence as PLI, except in reverse, EC decreases with increasing oxygen content whereas PLI increases.

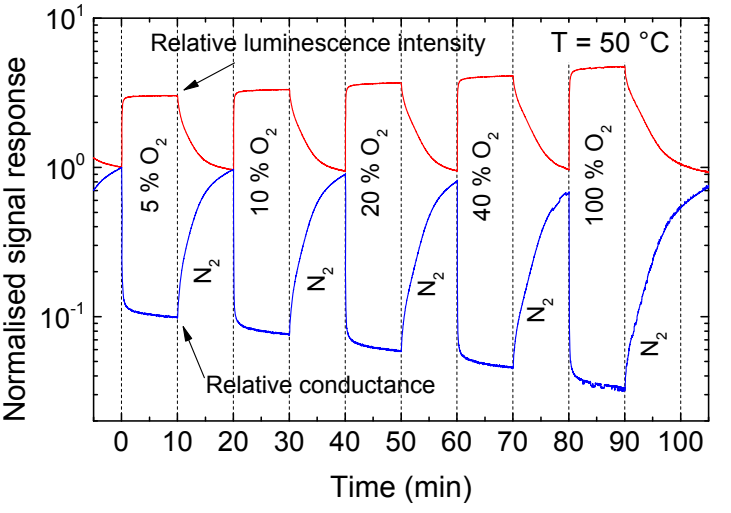

Fig. 19. Temporal response of PL intensity and conductance signals to variations of oxygen content in the surrounding atmosphere. The values are relative to the response signal value at $t = 0$.

For each time point in Fig 19. we have two signal values that can both be separately plotted against time but can also be plotted against each other, as demonstrated in Fig 20. It turns out that there is a strong relationship between PL intensity and EC. The relationship is somewhat similar to a power law:

$$y = ax^b \tag{19}$$

Such a law would yield a straight line in a log-log plot, as

$$\log(y) = \log(A) + b * \log(x) \tag{20}$$

is a linear function with respect to $\log(y)$ and $\log(x)$. Note that although mathematically equations 1 and 8 are identical, their physical meaning is different. Eq. 1 establishes a relationship between sensor signal and measurand (gas concentration), but Eq. 8 is a relationship between two sensor signals.

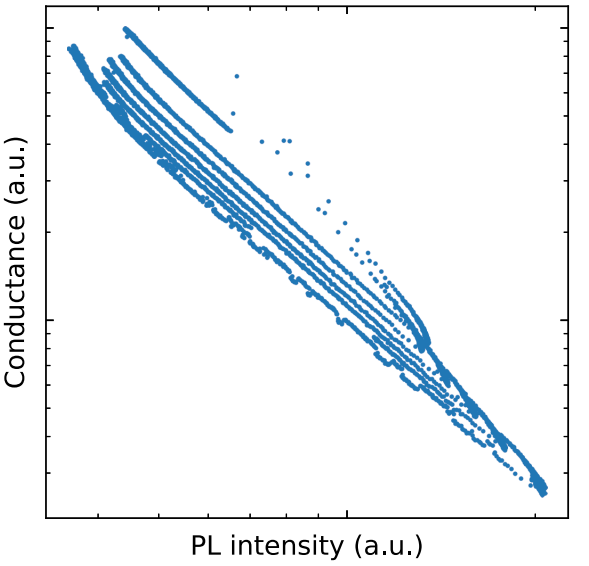

Fig. 20. The data points from Fig 19, with PL intensity and conductance plotted against each other.

Fig 20 clearly reveals that the relationship is not perfect and the different oxygen cycles each draw a separate near power law line on the plot that does not exactly match the line drawn by the previous cycle. If the relationship between PL intensity and EC would follow a fixed curve, then the two signals would essentially carry the same information since one signal can be converted to another via some kind of a function. However, in our case such function does not exist, meaning that measuring both signals might introduce some new information.

Therefore, the main goal of this chapter is to show that measuring PL intensity and EC simultaneously and combining the two signals in a suitable way for the estimation of oxygen concentration gives an advantage over the traditional setup, where (oxygen) gas concentration is calculated from a single signal only. The advantage in our case is that the sensor becomes more precise.

6.2. The experiment with a pseudorandom gas sequence

To see how PL intensity, EC and both combined perform as sensor signals, I could create a sensor calibration based on each and then estimate the precision of each of the calibrations. Unfortunately the data presented in Fig 20 is not well suited for such a task, as the oxygen concentration changes abruptly (Fig 19) and covers only some fixed values. Between the oxygen cycles, the material was exposed to pure nitrogen, supposedly corresponding to precisely 0 % oxygen, but this is somewhat vague as there is always some oxygen contamination present. Moreover, the actual gas concentration close to material surface after the gas change is not very well defined, as it takes some time to replace the gas in the experiment chamber. Lastly, such abrupt concentration changes rarely occur in a real life scenario.

Taking into account the previous argumentation, I devised a new oxygen test cycle, where the oxygen concentration varied randomly and continuously between 21 % and 0.21 % over the course of more than 50 hours (Fig 21).

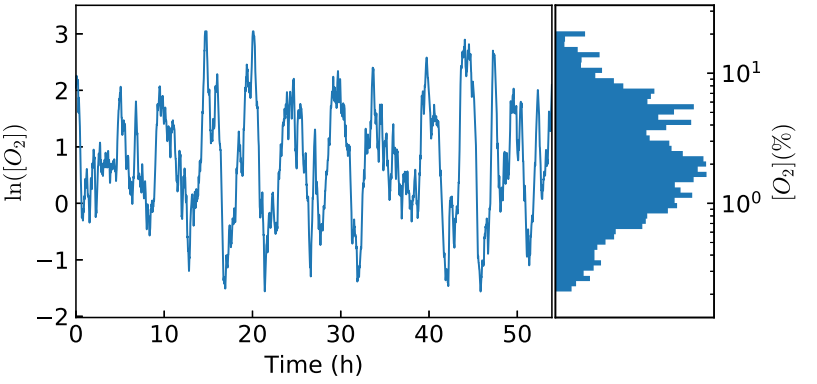

Fig. 21. The temporal profile of the random oxygen program.

This smooth test program is somewhat more similar to what the sensor might experience in real life and it fully covers a range of oxygen concentrations, being much better suitable for the calibration of the sensor and subsequent precision estimation.

The temporal responses to this random test program are depicted in Fig 22a. The dependence between PL intensity and EC follows a power law pattern similar to Fig 20 and there is also a drift present, the points cover an area rather than a line.

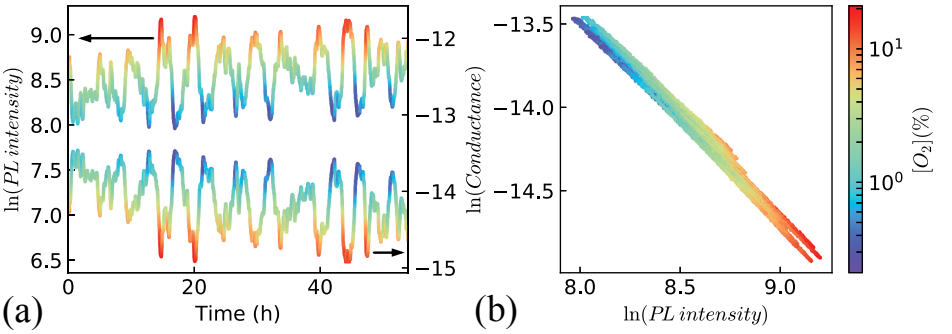

Fig. 22. a) The temporal response of the material to the random test program (introduced in Fig 21). b) The two response signals, PL intensity and EC, plotted against each other. Colour encodes oxygen concentration at the particular point.

Now that we have a rather wide range of oxygen concentrations continuously covered, it is possible to plot the response signals against oxygen concentration (Fig. 23). In case of a perfect sensor, we would have a linear one-to-one relationship between the response signal and the measurand. In our case, the relationship is clearly not a one-to-one line, meaning that a single PL intensity or EC value can correspond to a range of oxygen concentrations – limiting the sensor precision. However, the relationship is somewhat linear in a log-log space and based on that observation I performed the rest of the calibration and analysis based on the logarithms of PL intensity, EC and oxygen concentration.

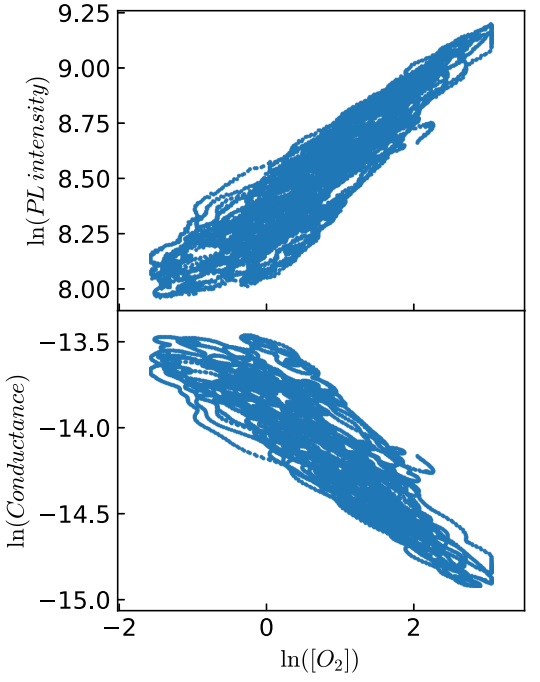

Fig. 23. The relationship between PL intensity and EC against time. The relationships are ambiguous and as a first approximation linear in a log-log space.

At this point we are ready to create the actual sensor calibrations and see how well they perform. A calibration is a mathematical model that converts the output parameter of the sensor (logarithms of PL intensity and/or EC) to the measurand (logarithm of oxygen concentration):

$$\log(p[O_2]) = f_p(\log(S_{PL})) \tag{21}$$

$$\log(p[\mathrm{O}_2]) = f_c(\log(S_{\mathrm{EC}})) \tag{22}$$

$$\log(p[\mathrm{O}_2]) = f_{pc}\big((\log(S_{\mathrm{PL}}), \log(S_{EC})\big) \tag{23}$$

where $p[\mathrm{O}_2]$ is the predicted oxygen concentration, S_{PL} is PL intensity signal value, S_{EC} is the EC signal value and f_p, f_c and f_{pc} are the calibration models for PL intensity, EC and both respectively. To show that using PL intensity and EC simultaneously in a calibration model provides an advantage I have to show that there is some form of f_{pc} always outperforms f_p and f_c regardless of the choice of the latter two.

To see how well the three calibration models perform we have to give them a concrete mathematical form. One of the most straightforward approaches for this is a polynomial linear regression model where the parameters of the model can be determined using the least squares method. The mathematical forms of the models are as follows:

$$\mathrm{z} = \sum_{i=0}^{n} a_i x^i \tag{24}$$

$$\mathrm{z} = \sum_{0 \le i+j \le n} a_{i,j} x^i y^j = \sum_{k=0}^{n} \sum_{i=0}^{k} a_{i,k-i} x^i y^{k-i} \tag{25}$$

for the one and two parameter models respectively, where z is the output of the model ($\log(p[O_2])$ in the present case), x and y are the (logarithms of the) input signals and n is the order of the polynomial. The larger the n parameter, the more complex forms the model can take. Theoretically the polynomial model can fit arbitrarily complex functions. This is an important property, because we want to avoid a situation where a calibration model performs poorly not because of physical limitations of the material but rather the nonflexibility of the model's chosen mathematical form. The a parameters in the model are determined with the least squares method using experimental data. This process is called training the model.

An inherent limitation of high order polynomials is that they tend to output absurd values when their input parameters are not in the region that was covered by the data that was used for training the polynomial model. In a real sensor

application this might be the case because the sensor properties can drift during the lifetime of the sensor. Altogether this means that if possible, lower order polynomial models should be used.

It is also important to use different data sets for training the models and for testing the model performance – precision in the present case. When using the same data for training and testing there is the risk of fitting noise – by increasing the complexity of the model its apparent precision increases, but the increase comes from adjusting to fluctuations in the data that are characteristic of the training set and not the measurement data and the physical processes behind it in general. Therefore, I split the data in half, I used the first 60 % of the points for training and the remaining 40 % for precision testing the model. In the context of gas sensors it is actually rather natural because in real applications the sensor is first calibrated and then put to work, recalibrating after the sensor has been deployed is usually not possible.

Finally, I have to define a method for estimating the error of the model. I chose the relative root mean square:

$$error = \sqrt{\sum_{i=0}^{m} \left(\frac{p[\mathrm{O}_2]_i - t[\mathrm{O}_2]_i}{t[\mathrm{O}_2]_i} \right)^2} \tag{26}$$

where $p[\mathrm{O}_2]$ is the oxygen concentration predicted by the model, $t[\mathrm{O}_2]$ is the true oxygen concentration and m is the number of data points in the test set. Since the training of the model is done using logarithms then the relative root mean square is minimised using the least squares method.

At this point we have clarified all the details needed to proceed with the analysis. The procedure is as follows: first, I split the data into 60 % training and 40% test sets. Then I train three different polynomial models that establish a relationship between some of the sensor response signals and oxygen concentration: two single parameter polynomial models for both PL intensity and EC (according to Eq. 7) and one double parameter polynomial model that uses both PL intensity and EC (according to Eq. 8). I use the models to predict oxygen concentrations for all the data points in the test set and then calculate the error of the model using the true oxygen concentration values and Eq. 9. I start with polynomial order $n = 1$ and increase n until the error stops decreasing.

Table 2 lists the results the described process. When the PL intensity or EC signals where used separately, we obtained the best results with the first order polynomial model. This indicates that the use of logarithms in the models is justified as the relationship between the logarithms of PL intensity and EC vs the logarithm of oxygen concentration is indeed near linear. When PL intensity and EC were used simultaneously in a single model, then the second order polynomial gave the best result. It is also notable that the best result of the PL+EC model was more than twice as good as the best result of the PL or EC

models. This gives a quantitative justification of using the two parameters at the same time and proves the hypothesis proposed in the beginning of this chapter.

Table 2. The relative root mean square errors of different models with different polynomial ranks.

	PL	EC	PL+EC
1	0.694	0.893	0.356
2	0.710	0.908	0.292
3	0.721	0.920	0.413
4	0.721	0.925	0.356
5	0.721	0.925	0.501
6	0.721	0.925	0.501

A further insight into the behaviour of the models is given by the temporal profile of the relative errors (Fig. 24). In this plot the relative errors of the best performing models are plotted against time. Models with different input response signals are plotted separately. The whole data set is plotted including both the training set and the test set, separated by the red line. The illustration reveals a certain drift of the signals that is particularly noticeable in case of models with a single input signal. A consequence of the drift is that the during the test period the model slowly becomes inaccurate, meaning that the sensor requires recalibration. The dual response model manages to counter the drift much better, as the errors are roughly centred around zero not only in the training set but also in the test set.

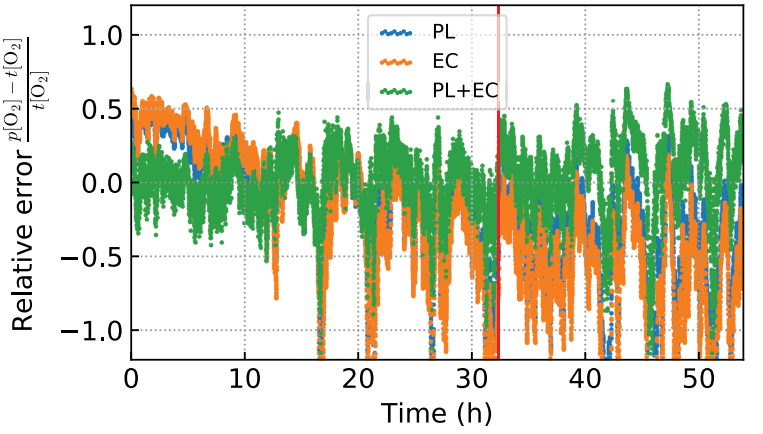

Fig. 24. The temporal evolution of the relative errors of models using PL intensity, EC and both as input signals. The best model (according to Table 2) is depicted for each input signals. The red line separates the training and test sets.

Finally, the dual response calibration models can be visualised (Fig 25). In the visualisation, the data points are from experimental data, the same as in Fig 22b. The solid fill under the data points is the output of the polynomial model. The first and second order models are visualised. In case of an ideal model, the experiment points should be nearly invisible on the background. The visualisation also demonstrates the stability of the first order model and the flexibility of the second order model, which was the most precise.

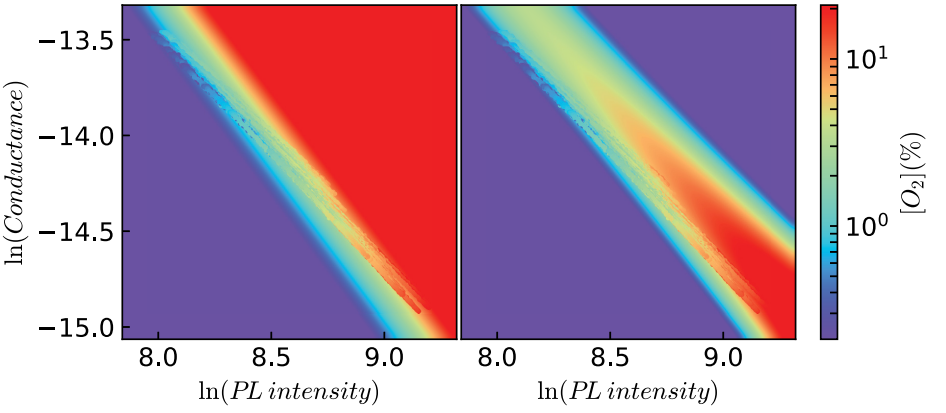

Fig. 25. The dual response models visualised together with experimental data points. The data points are the same as in Fig. 22b and the solid fill is the response of the model. First (a) and second (b) order polynomial models are displayed. The colour scale is clipped at the extreme values of the experiment.

6.3. Conclusions

The TiO_2:Sm^{3+} sensor material exhibits a dual response behaviour which means that PLI and EC that both act as sensor response signals can be recorded simultaneously from a single body of the sensing material. Both signals can be separately used to determine the ambient oxygen concentration, however combining them both allows us to increase the precision of the oxygen concentration readout by more than two times.

7. SUMMARY

The primary aim of this work was to obtain a thorough understanding of the properties and capabilities of the TiO_2:Sm^{3+} material as the transducer of an optical oxygen gas sensor. The main achievements regarding this aim are as follows:

1. **Sensing material:** The morphology and phase of the of the TiO_2:Sm^{3+} powders were studied and documented revealing it to be in anatase phase and consisting of agglomerated 40 nm crystallites. A method was devised to assemble the powder into stable and durable samples suitable for both optical and electrical measurements. The key aspects of electrical and optical properties of the samples were characterised. The material had a PL spectrum typical of Sm^{3+} with characteristic peaks in the red-orange part of the visible spectrum. The optical bandgap of the material was 3.27 eV. Electrical measurements suggest that the surface chemistry of the material is heavily influenced by UV illumination.
2. **PL based gas sensing**: The optical gas sensing capabilities of the material were investigated using dedicated gas sensor test equipment. Namely, the response of PL intensity to oxygen gas was studied and the response time and stationary response curve was estimated. The material showed good oxygen sensing capabilities starting from 100 % oxygen down to 0.01 % and possibly below. In addition, the response of PL decays to oxygen gas was investigated. The decays showed similar oxygen sensing capabilities. Mathematical modelling was applied on the decays to determine the mechanisms responsible for the PL oxygen dependence. It was found that changes in ambient oxygen concentration lead to a change of PL quenching centre concentration that in turn leads to a change of effective decay rate. The sensitivity of the material can be enhanced by increasing the concentration of the quenching centres.
3. **Dual response:** A method to record both PL intensity and EC of the material simultaneously in a so called dual response mode was developed. To assess the practical aspects of this dual mode sensing a test scenario somewhat simulating real working conditions was developed. The dual sensor response data of the test scenario was utilised to perform a mathematical analysis of the performance of the output signals. The analysis revealed that it is possible to combine the two output signals in such a way that the precision of the sensor increases two times.

SUMMARY IN ESTONIAN

Samaariumiga dopeeritud TiO_2 optilise ja mitmekostelise hapnikutundlikkuse analüüs

See töö keskendub samaariumi ioonidega (Sm^{3+}) dopeeritud titaandioksiidi (TiO_2:Sm^{3+}) optiliste gaasisensoromaduste kaardistamisele. Metalloksiididel põhinevad pooljuhtgaasisensorid – kuhu TiO_2 kuulub – on laialdaselt uuritud sensormaterjalide klass. Need gaasisensorid on lihtsa ehitusega, odavad, hea tundlikkuse ja stabiilsusega. Seetõttu on tööstusel ja teadusel jätkuv huvi selle materjaliklassi vastu.

Klassikalised pooljuhtgaasisensorid põhinevad elektrilisel kostel, mis tähendab, et sensori väljundsignaaliks on tema elektriline takistus. Sõltuvalt gaasikeskkonna koostisest takistus muutub ja seetõttu on takistust mõõtes võimalik määrata mõõdetavate gaaside kontsentratsiooni sensorit ümbritsevas gaasikeskkonnas. Siin uuritud materjal erineb klassikalistest pooljuhtgaasisensoritest selle poolest, et kosteks on optiline signaal. Mõõdetavaks optiliseks suuruseks on fotoluminestsentsi intensiivsus või ka selle kustumise kiirus. Antud töö tegeleb sensormaterjali hapnikutundlikkuse uurimisega. Hapnik on hea indikaatorgaas, mida on ühest küljest lihtne ja odav eksperimentides kasutada, aga teisest küljest kaasneb hapnikutundlikkusega üldjuhul ka tundlikkus teistele olulistele gaasidele.

Uuritav TiO_2:Sm^{3+} materjal koosnes anataasi nanokristalliitidest, mille läbimõõt oli ligikaudu 40 nm. Kristalliidid olid tugevalt aglomereerunud ja moodustasid valge nanopulbri. Ultraviolettkiirgusega kiiritamisel tekkis materjalis punakas-oranž fotoluminestsents, mille kiirgusspekter koosnes samaariumile iseloomulikest joontest. Materjali hinnanguline optiline keelutsooni laius oli 3.27 eV.

Materjali fotoluminestsentsi intensiivsus sõltus tugevalt materjali ümbritseva gaasikeskkonna hapniku kontsentratsioonist. Fotoluminestsentsi intensiivsuse abil oli hapniku kontsentratsiooni võimalik hinnata vahemikus 0.01% kuni 100%, kusjuures alumist piiri on tõenäoliselt võimalik veel vähendada. Ka fotoluminestsentsi kustumiskineetika sõltus hapniku kontsentratsioonist. Kustumiskineetikate matemaatiline analüüs näitas, et fotoluminestsentsi hapnikutundlikkuse põhjustab luminestsentsi kustutavate tsentrite kontsentratsiooni muutus sensormaterjalis pinnale adsorbeerunud hapniku mõjul.

TiO_2 on kasutuses elektrilistes gaasisensorites ja seetõttu uuriti selles töös ka TiO_2:Sm^{3+} toimimist nö kahekostelises režiimis, kus paralleelselt registreeritakse nii optiline kui ka elektriline signaal. Elektriliseks signaaliks oli materjali elektriline juhtivus. Selgus, et optilise ja elektrilise signaali vahel on tugev korrelatsioon, kusjuures mõlemad signaalid on kõlbulikud keskkonna hapnikusisalduse hindamiseks. Seejärel võrreldi signaalide täpsust hapniku kontsentratsiooni hindamisel, mille tulemusel selgus, et nii optilise kui ka elektrilise signaali täpsus on sarnane. Teisalt selgus, et kahe signaali samaaegne arvesse võtmine võimaldab hapniku sisaldust keskkonnas rohkem kui kaks korda täpsemalt hinnata. Täpsuse hindamiseks kasutatud metoodikat saab rakendada ka muude mitmekosteliste sensorite täpsuse analüüsiks.

REFERENCES

[1] O. S. Wolfbeis, “Luminescent sensing and imaging of oxygen: Fierce competition to the Clark electrode,” *BioEssays*, vol. 37, no. 8, pp. 921–928, Aug. 2015. https://doi.org/10.1002/bies.201500002

[2] J. R. Lakowicz, *Principles of Fluorescence Spectroscopy*, 3rd ed. Springer US, 2006.

[3] X. Wang and O. S. Wolfbeis, “Optical methods for sensing and imaging oxygen: materials, spectroscopies and applications,” *Chem. Soc. Rev.*, vol. 43, no. 10, pp. 3666–3761, Apr. 2014. https://doi.org/10.1039/C4CS00039K

[4] E. J. Bowen and A. Norton, “The quenching of fluorescence in solution,” *Trans. Faraday Soc.*, vol. 35, no. 0, pp. 44–48, Jan. 1939. https://doi.org/10.1039/TF9393500044

[5] S. Kochmann, C. Baleizão, M. N. Berberan-Santos, and O. S. Wolfbeis, “Sensing and Imaging of Oxygen with Parts per Billion Limits of Detection and Based on the Quenching of the Delayed Fluorescence of 13C70 Fullerene in Polymer Hosts,” *Anal. Chem.*, vol. 85, no. 3, pp. 1300–1304, Feb. 2013. https://doi.org/10.1021/ac303486f

[6] G. Korotcenkov, “Metal oxides for solid-state gas sensors: What determines our choice?,” *Materials Science and Engineering: B*, vol. 139, no. 1, pp. 1–23, Apr. 2007. https://doi.org/10.1016/j.mseb.2007.01.044

[7] N. Barsan and U. Weimar, “Conduction Model of Metal Oxide Gas Sensors,” *Journal of Electroceramics*, vol. 7, no. 3, pp. 143–167, Dec. 2001. https://doi.org/10.1023/A:1014405811371

[8] K. Komaguchi, T. Maruoka, H. Nakano, I. Imae, Y. Ooyama, and Y. Harima, “Electron-Transfer Reaction of Oxygen Species on TiO2 Nanoparticles Induced by Sub-band-gap Illumination,” *J. Phys. Chem. C*, vol. 114, no. 2, pp. 1240–1245, Jan. 2010. https://doi.org/10.1021/jp909678e

[9] M. Che and A. J. Tench, “Characterization and Reactivity of Molecular Oxygen Species on Oxide Surfaces,” in *Advances in Catalysis*, vol. 32, D. D. Eley, H. Pines, and P. B. Weisz, Eds. Academic Press, 1983, pp. 1–148. https://doi.org/10.1016/S0360-0564(08)60439-3

[10] E. Carter, A. F. Carley, and D. M. Murphy, “Evidence for O2- Radical Stabilization at Surface Oxygen Vacancies on Polycrystalline TiO2,” *J. Phys. Chem. C*, vol. 111, no. 28, pp. 10630–10638, Jul. 2007. https://doi.org/10.1021/jp0729516

[11] M. A. Henderson, W. S. Epling, C. L. Perkins, C. H. F. Peden, and U. Diebold, “Interaction of Molecular Oxygen with the Vacuum-Annealed TiO2(110) Surface: Molecular and Dissociative Channels,” *J. Phys. Chem. B*, vol. 103, no. 25, pp. 5328–5337, Jun. 1999. https://doi.org/10.1021/jp990655q

[12] N. Yamazoe, J. Fuchigami, M. Kishikawa, and T. Seiyama, “Interactions of tin oxide surface with O2, H2O AND H2,” *Surface Science*, vol. 86, pp. 335–344, Jul. 1979. https://doi.org/10.1016/0039-6028(79)90411-4

[13] M. E. Franke, T. J. Koplin, and U. Simon, “Metal and Metal Oxide Nanoparticles in Chemiresistors: Does the Nanoscale Matter?,” *Small*, vol. 2, no. 1, pp. 36–50, 2006. https://doi.org/10.1002/smll.200500261

[14] T. Liu, X. Zhang, L. Yuan, and J. Yu, “A review of high-temperature electrochemical sensors based on stabilized zirconia,” *Solid State Ionics*, vol. 283, pp. 91–102, Dec. 2015. https://doi.org/10.1016/j.ssi.2015.10.012

[15] J. Riegel, H. Neumann, and H.-M. Wiedenmann, “Exhaust gas sensors for automotive emission control,” *Solid State Ionics*, vol. 152–153, pp. 783–800, Dec. 2002. https://doi.org/10.1016/S0167-2738(02)00329-6

[16] N. Barsan, M. Schweizer-Berberich, and W. Göpel†, “Fundamental and practical aspects in the design of nanoscaled SnO2 gas sensors: a status report,” *Fresenius J Anal Chem*, vol. 365, no. 4, pp. 287–304, Oct. 1999. https://doi.org/10.1007/s002160051490

[17] N. Yamazoe and K. Shimanoe, “Theory of power laws for semiconductor gas sensors,” *Sensors and Actuators B: Chemical*, vol. 128, no. 2, pp. 566–573, Jan. 2008. https://doi.org/10.1016/j.snb.2007.07.036

[18] H.-J. Kim and J.-H. Lee, “Highly sensitive and selective gas sensors using p-type oxide semiconductors: Overview,” *Sensors and Actuators B: Chemical*, vol. 192, pp. 607–627, Mar. 2014. https://doi.org/10.1016/j.snb.2013.11.005

[19] M. M. Arafat, B. Dinan, S. A. Akbar, and A. S. M. A. Haseeb, “Gas Sensors Based on One Dimensional Nanostructured Metal-Oxides: A Review,” *Sensors*, vol. 12, no. 6, pp. 7207–7258, May 2012. https://doi.org/10.3390/s120607207

[20] M. Batzill, “Surface Science Studies of Gas Sensing Materials: SnO2,” *Sensors*, vol. 6, no. 10, pp. 1345–1366, Oct. 2006. https://doi.org/10.3390/s6101345

[21] M. Batzill and U. Diebold, “The surface and materials science of tin oxide,” *Progress in Surface Science*, vol. 79, no. 2, pp. 47–154, Jan. 2005. https://doi.org/10.1016/j.progsurf.2005.09.002

[22] T. Seiyama, A. Kato, K. Fujiishi, and M. Nagatani, “A New Detector for Gaseous Components Using Semiconductive Thin Films.,” *Anal. Chem.*, vol. 34, no. 11, pp. 1502–1503, Oct. 1962. https://doi.org/10.1021/ac60191a001

[23] R. Kumar, O. Al-Dossary, G. Kumar, and A. Umar, “Zinc Oxide Nanostructures for NO<Subscript>2</Subscript> Gas–Sensor Applications: A Review,” *Nano-Micro Lett.*, vol. 7, no. 2, pp. 97–120, Apr. 2015. https://doi.org/10.1007/s40820-014-0023-3

[24] E. Comini, C. Baratto, G. Faglia, M. Ferroni, and G. Sberveglieri, “Single crystal ZnO nanowires as optical and conductometric chemical sensor,” *J. Phys. D: Appl. Phys.*, vol. 40, no. 23, p. 7255, 2007. https://doi.org/10.1088/0022-3727/40/23/S08

[25] L. Liao, H. B. Lu, J. C. Li, H. He, D. F. Wang, D. J. Fu, C. Liu, and W. F. Zhang, “Size Dependence of Gas Sensitivity of ZnO Nanorods,” *J. Phys. Chem. C*, vol. 111, no. 5, pp. 1900–1903, Feb. 2007. https://doi.org/10.1021/jp065963k

[26] G. S. T. Rao and D. Tarakarama Rao, “Gas sensitivity of ZnO based thick film sensor to NH3 at room temperature,” *Sensors and Actuators B: Chemical*, vol. 55, no. 2–3, pp. 166–169, May 1999. https://doi.org/10.1016/S0925-4005(99)00049-0

[27] A. Wei, L. Pan, and W. Huang, “Recent progress in the ZnO nanostructure-based sensors,” *Materials Science and Engineering: B*, vol. 176, no. 18, pp. 1409–1421, Nov. 2011. https://doi.org/10.1016/j.mseb.2011.09.005

[28] J. Lee, D. H. Kim, S.-H. Hong, and J. Y. Jho, “A hydrogen gas sensor employing vertically aligned TiO2 nanotube arrays prepared by template-assisted method,” *Sensors and Actuators B: Chemical*, vol. 160, no. 1, pp. 1494–1498, Dec. 2011. https://doi.org/10.1016/j.snb.2011.08.001

[29] I.-D. Kim, A. Rothschild, B. H. Lee, D. Y. Kim, S. M. Jo, and H. L. Tuller, “Ultrasensitive Chemiresistors Based on Electrospun TiO2 Nanofibers,” *Nano Lett.*, vol. 6, no. 9, pp. 2009–2013, Sep. 2006. https://doi.org/10.1021/nl061197h

[30] K. Galatsis, Y. X. Li, W. Wlodarski, E. Comini, G. Sberveglieri, C. Cantalini, S. Santucci, and M. Passacantando, “Comparison of single and binary oxide MoO3, TiO2 and WO3 sol–gel gas sensors,” *Sensors and Actuators B: Chemical*, vol. 83, no. 1, pp. 276–280, Mar. 2002. https://doi.org/10.1016/S0925-4005(01)01072-3

[31] X. Wang, N. Miura, and N. Yamazoe, “Study of WO3-based sensing materials for NH3 and NO detection,” *Sensors and Actuators B: Chemical*, vol. 66, no. 1, pp. 74–76, Jul. 2000. https://doi.org/10.1016/S0925-4005(99)00410-4

[32] Y. S. Kim, S.-C. Ha, K. Kim, H. Yang, S.-Y. Choi, Y. T. Kim, J. T. Park, C. H. Lee, J. Choi, J. Paek, and K. Lee, “Room-temperature semiconductor gas sensor based on nonstoichiometric tungsten oxide nanorod film,” *Applied Physics Letters*, vol. 86, no. 21, p. 213105, May 2005. https://doi.org/10.1063/1.1929872

[33] S. Fardindoost, A. Iraji zad, F. Rahimi, and R. Ghasempour, “Pd doped WO3 films prepared by sol–gel process for hydrogen sensing,” *International Journal of Hydrogen Energy*, vol. 35, no. 2, pp. 854–860, Jan. 2010. https://doi.org/10.1016/j.ijhydene.2009.11.033

[34] M. Penza, C. Martucci, and G. Cassano, “NOx gas sensing characteristics of WO3 thin films activated by noble metals (Pd, Pt, Au) layers,” *Sensors and Actuators B: Chemical*, vol. 50, no. 1, pp. 52–59, Jul. 1998. https://doi.org/10.1016/S0925-4005(98)00156-7

[35] K. Persaud and G. Dodd, “Analysis of discrimination mechanisms in the mammalian olfactory system using a model nose,” *Nature*, vol. 299, no. 5881, pp. 352–355, Sep. 1982. https://doi.org/10.1038/299352a0

[36] F. Röck, N. Barsan, and U. Weimar, “Electronic Nose: Current Status and Future Trends,” *Chem. Rev.*, vol. 108, no. 2, pp. 705–725, Feb. 2008. https://doi.org/10.1021/cr068121q

[37] L. M. Reid, C. P. O’Donnell, and G. Downey, “Recent technological advances for the determination of food authenticity,” *Trends in Food Science & Technology*, vol. 17, no. 7, pp. 344–353, Jul. 2006. https://doi.org/10.1016/j.tifs.2006.01.006

[38] S. J. Toal and W. C. Trogler, “Polymer sensors for nitroaromatic explosives detection,” *J. Mater. Chem.*, vol. 16, no. 28, pp. 2871–2883, Jul. 2006. https://doi.org/10.1039/B517953J

[39] F. D. Francesco, B. Lazzerini, F. Marcelloni, and G. Pioggia, “An electronic nose for odour annoyance assessment,” *Atmospheric Environment*, vol. 35, no. 7, pp. 1225–1234, Jan. 2001. https://doi.org/10.1016/S1352-2310(00)00392-7

[40] C. Di Natale, A. Macagnano, E. Martinelli, R. Paolesse, G. D’Arcangelo, C. Roscioni, A. Finazzi-Agrò, and A. D’Amico, “Lung cancer identification by the analysis of breath by means of an array of non-selective gas sensors,” *Biosensors and Bioelectronics*, vol. 18, no. 10, pp. 1209–1218, Sep. 2003. https://doi.org/10.1016/S0956-5663(03)00086-1

[41] R. F. Machado, D. Laskowski, O. Deffenderfer, T. Burch, S. Zheng, P. J. Mazzone, T. Mekhail, C. Jennings, J. K. Stoller, J. Pyle, J. Duncan, R. A. Dweik, and S. C. Erzurum, “Detection of Lung Cancer by Sensor Array Analyses of Exhaled Breath,” *Am J Respir Crit Care Med*, vol. 171, no. 11, pp. 1286–1291, Jun. 2005. https://doi.org/10.1164/rccm.200409-1184OC

[42] C. Di Natale, R. Paolesse, E. Martinelli, and R. Capuano, “Solid-state gas sensors for breath analysis: A review,” *Analytica Chimica Acta*, vol. 824, pp. 1–17, May 2014. https://doi.org/10.1016/j.aca.2014.03.014

[43] B. Guo, A. Bermak, P. C. H. Chan, and G.-Z. Yan, "A monolithic integrated 4×4 tin oxide gas sensor array with on-chip multiplexing and differential readout circuits," *Solid-State Electronics*, vol. 51, no. 1, pp. 69–76, Jan. 2007. https://doi.org/10.1016/j.sse.2006.10.015

[44] P.-C. Chen, F. N. Ishikawa, H.-K. Chang, K. Ryu, and C. Zhou, "A nano-electronic nose: a hybrid nanowire/carbon nanotube sensor array with integrated micromachined hotplates for sensitive gas discrimination," *Nanotechnology*, vol. 20, no. 12, p. 125503, 2009. https://doi.org/10.1088/0957-4484/20/12/125503

[45] R. Beccherelli, E. Zampetti, S. Pantalei, M. Bernabei, and K. C. Persaud, "Design of a very large chemical sensor system for mimicking biological olfaction," *Sensors and Actuators B: Chemical*, vol. 146, no. 2, pp. 446–452, Apr. 2010. https://doi.org/10.1016/j.snb.2009.11.031

[46] S. M. Scott, D. James, and Z. Ali, "Data analysis for electronic nose systems," *Microchim Acta*, vol. 156, no. 3–4, pp. 183–207, Dec. 2006. https://doi.org/10.1007/s00604-006-0623-9

[47] K. L. Goodner, J. G. Dreher, and R. L. Rouseff, "The dangers of creating false classifications due to noise in electronic nose and similar multivariate analyses," *Sensors and Actuators B: Chemical*, vol. 80, no. 3, pp. 261–266, Dec. 2001. https://doi.org/10.1016/S0925-4005(01)00917-0

[48] R. A. Potyrailo, "Multivariable Sensors for Ubiquitous Monitoring of Gases in the Era of Internet of Things and Industrial Internet," *Chem. Rev.*, vol. 116, no. 19, pp. 11877–11923, Oct. 2016. https://doi.org/10.1021/acs.chemrev.6b00187

[49] E. S. Snow and F. K. Perkins, "Capacitance and Conductance of Single-Walled Carbon Nanotubes in the Presence of Chemical Vapors," *Nano Lett.*, vol. 5, no. 12, pp. 2414–2417, Dec. 2005. https://doi.org/10.1021/nl051669c

[50] Y. Chen, H. Zhang, Z. Feng, H. Zhang, R. Zhang, Y. Yu, J. Tao, H. Zhao, W. Guo, W. Pang, X. Duan, J. Liu, and D. Zhang, "Chemiresistive and Gravimetric Dual-Mode Gas Sensor toward Target Recognition and Differentiation," *ACS Appl. Mater. Interfaces*, vol. 8, no. 33, pp. 21742–21749, Aug. 2016. https://doi.org/10.1021/acsami.6b02682

[51] B. Wang, J. C. Cancilla, J. S. Torrecilla, and H. Haick, "Artificial Sensing Intelligence with Silicon Nanowires for Ultraselective Detection in the Gas Phase," *Nano Lett.*, vol. 14, no. 2, pp. 933–938, Feb. 2014. https://doi.org/10.1021/nl404335p

[52] L. Giancaterini, C. Cantalini, M. Cittadini, M. Sturaro, M. Guglielmi, A. Martucci, A. Resmini, and U. Anselmi-Tamburini, "Au and Pt Nanoparticles Effects on the Optical and Electrical Gas Sensing Properties of Sol #x2013;Gel-Based ZnO Thin-Film Sensors," *IEEE Sensors Journal*, vol. 15, no. 2, pp. 1068–1076, Feb. 2015. https://doi.org/10.1109/JSEN.2014.2356252

[53] T. Jalkanen, J. Tuura, E. Mäkilä, and J. Salonen, "Electro-optical porous silicon gas sensor with enhanced selectivity," *Sensors and Actuators B: Chemical*, vol. 147, no. 1, pp. 100–104, May 2010. https://doi.org/10.1016/j.snb.2010.03.005

[54] M. Furuki and L. Sun Pu, "Hybrid gas detector of squarylium dye Langmuir-Blodgett film deposited on a quartz oscillator," *Thin Solid Films*, vol. 210–211, pp. 471–473, Apr. 1992. https://doi.org/10.1016/0040-6090(92)90315-3

[55] C. Baratto, G. Faglia, G. Sberveglieri, Z. Gaburro, L. Pancheri, C. Oton, and L. Pavesi, "Multiparametric Porous Silicon Sensors," *Sensors*, vol. 2, no. 3, pp. 121–126, Apr. 2002. https://doi.org/10.3390/s20300121

[56] H.-J. Kim, Y.-Y. Kim, and K.-W. Lee, “Multiparametric sensor based on DBR porous silicon for detection of ethanol gas,” *Current Applied Physics*, vol. 10, no. 1, pp. 181–183, Jan. 2010. https://doi.org/10.1016/j.cap.2009.04.020

[57] G. D. Francia, V. L. Ferrara, L. Quercia, and G. Faglia, “Sensitivity of Porous Silicon Photoluminescence to Low Concentrations of CH4 and CO,” *Journal of Porous Materials*, vol. 7, no. 1–3, pp. 287–290, Jan. 2000. https://doi.org/10.1023/A:1009640316318

[58] C. Baratto, E. Comini, G. Faglia, G. Sberveglieri, M. Zha, and A. Zappettini, “Metal oxide nanocrystals for gas sensing,” *Sensors and Actuators B: Chemical*, vol. 109, no. 1, pp. 2–6, Aug. 2005. https://doi.org/10.1016/j.snb.2005.03.091

[59] V. S. Nguyen, Y. Champouret, M. L. Kahn, V. Jubera, and H. Debéda, “Simultaneously Measured Photoluminescent and Conductive Properties of Printed ZnO Nanocrystals under Ar/O2 Mixtures,” *Procedia Engineering*, vol. 120, pp. 993–997, Jan. 2015. https://doi.org/10.1016/j.proeng.2015.08.641

[60] H. Tang, H. Berger, P. E. Schmid, F. Lévy, and G. Burri, “Photoluminescence in TiO2 anatase single crystals,” *Solid State Communications*, vol. 87, no. 9, pp. 847–850, Sep. 1993. https://doi.org/10.1016/0038-1098(93)90427-O

[61] C. B. Almquist and P. Biswas, “Role of Synthesis Method and Particle Size of Nanostructured TiO2 on Its Photoactivity,” *Journal of Catalysis*, vol. 212, no. 2, pp. 145–156, Dec. 2002. https://doi.org/10.1006/jcat.2002.3783

[62] J.-J. Wu and C.-C. Yu, “Aligned TiO2 Nanorods and Nanowalls,” *J. Phys. Chem. B*, vol. 108, no. 11, pp. 3377–3379, Mar. 2004. https://doi.org/10.1021/jp0361935

[63] A. Amtout and R. Leonelli, “Optical properties of rutile near its fundamental band gap,” *Phys. Rev. B*, vol. 51, no. 11, pp. 6842–6851, Mar. 1995. https://doi.org/10.1103/PhysRevB.51.6842

[64] L. Kavan, M. Grätzel, S. E. Gilbert, C. Klemenz, and H. J. Scheel, “Electrochemical and Photoelectrochemical Investigation of Single-Crystal Anatase,” *J. Am. Chem. Soc.*, vol. 118, no. 28, pp. 6716–6723, Jan. 1996. https://doi.org/10.1021/ja9541721

[65] H. Minoura, M. Nasu, and Y. Takahashi, “Comparative Studies of Photoelectrochemical Behaviours of Rutile and Anatase Electrodes Prepared by OMCVD Technique,” *Berichte der Bunsengesellschaft für physikalische Chemie*, vol. 89, no. 10, pp. 1064–1069, May 2010. https://doi.org/10.1002/bbpc.19850891010

[66] U. Diebold, “The surface science of titanium dioxide,” *Surface Science Reports*, vol. 48, no. 5, pp. 53–229, Jan. 2003. https://doi.org/10.1016/S0167-5729(02)00100-0

[67] V. Kiisk, M. Šavel, V. Reedo, A. Lukner, and I. Sildos, “Anatase-to-rutile phase transition of samarium-doped TiO2 powder detected via the luminescence of Sm3+,” *Physics Procedia*, vol. 2, no. 2, pp. 527–538, Aug. 2009. https://doi.org/10.1016/j.phpro.2009.07.038

[68] G. Colón, M. Maicu, M. C. Hidalgo, and J. A. Navío, “Cu-doped TiO2 systems with improved photocatalytic activity,” *Applied Catalysis B: Environmental*, vol. 67, no. 1, pp. 41–51, Sep. 2006. https://doi.org/10.1016/j.apcatb.2006.03.019

[69] P. Periyat, S. C. Pillai, D. E. McCormack, J. Colreavy, and S. J. Hinder, “Improved High-Temperature Stability and Sun-Light-Driven Photocatalytic Activity of Sulfur-Doped Anatase TiO2,” *J. Phys. Chem. C*, vol. 112, no. 20, pp. 7644–7652, May 2008. https://doi.org/10.1021/jp0774847

[70] O. Carp, C. L. Huisman, and A. Reller, “Photoinduced reactivity of titanium dioxide,” *Progress in Solid State Chemistry*, vol. 32, no. 1, pp. 33–177, Jan. 2004. https://doi.org/10.1016/j.progsolidstchem.2004.08.001

[71] A. Fujishima and X. Zhang, “Titanium dioxide photocatalysis: present situation and future approaches,” *Comptes Rendus Chimie*, vol. 9, no. 5, pp. 750–760, May 2006. https://doi.org/10.1016/j.crci.2005.02.055

[72] S. V. Eliseeva and J.-C. G. Bünzli, “Lanthanide luminescence for functional materials and bio-sciences,” *Chem. Soc. Rev.*, vol. 39, no. 1, pp. 189–227, Dec. 2009. https://doi.org/10.1039/B905604C

[73] S. I. Weissman, “Intramolecular Energy Transfer The Fluorescence of Complexes of Europium,” *The Journal of Chemical Physics*, vol. 10, no. 4, pp. 214–217, Apr. 1942. https://doi.org/10.1063/1.1723709

[74] P. Mukherjee, C. M. Shade, A. M. Yingling, D. N. Lamont, D. H. Waldeck, and S. Petoud, “Lanthanide Sensitization in II−VI Semiconductor Materials: A Case Study with Terbium(III) and Europium(III) in Zinc Sulfide Nanoparticles,” *J. Phys. Chem. A*, vol. 115, no. 16, pp. 4031–4041, Apr. 2011. https://doi.org/10.1021/jp109786w

[75] A. Chakraborty, G. H. Debnath, N. R. Saha, D. Chattopadhyay, D. H. Waldeck, and P. Mukherjee, “Identifying the Correct Host–Guest Combination To Sensitize Trivalent Lanthanide (Guest) Luminescence: Titanium Dioxide Nanoparticles as a Model Host System,” *J. Phys. Chem. C*, vol. 120, no. 41, pp. 23870–23882, Oct. 2016. https://doi.org/10.1021/acs.jpcc.6b08421

[76] K. L. Frindell, M. H. Bartl, M. R. Robinson, G. C. Bazan, A. Popitsch, and G. D. Stucky, “Visible and near-IR luminescence via energy transfer in rare earth doped mesoporous titania thin films with nanocrystalline walls,” *Journal of Solid State Chemistry*, vol. 172, no. 1, pp. 81–88, Apr. 2003. https://doi.org/10.1016/S0022-4596(02)00126-3

[77] M. G. Brik, I. Sildos, and V. Kiisk, “First-principles calculations of optical and electronic properties of pure and Sm3+-doped TiO2,” *Physica B: Condensed Matter*, vol. 405, no. 10, pp. 2450–2456, May 2010. https://doi.org/10.1016/j.physb.2010.03.006

[78] G. Faglia, C. Baratto, G. Sberveglieri, M. Zha, and A. Zappettini, “Adsorption effects of NO_2 at ppm level on visible photoluminescence response of SnO_2 nanobelts,” *Applied Physics Letters*, vol. 86, no. 1, p. 011923, Jan. 2005. https://doi.org/10.1063/1.1849832

[79] A. Setaro, A. Bismuto, S. Lettieri, P. Maddalena, E. Comini, S. Bianchi, C. Baratto, and G. Sberveglieri, “Optical sensing of NO2 in tin oxide nanowires at sub-ppm level,” *Sensors and Actuators B: Chemical*, vol. 130, no. 1, pp. 391–395, Mar. 2008. https://doi.org/10.1016/j.snb.2007.09.015

[80] V. M. Zhyrovetsky, D. I. Popovych, S. S. Savka, and A. S. Serednytski, “Nanopowder Metal Oxide for Photoluminescent Gas Sensing,” *Nanoscale Research Letters*, vol. 12, p. 132, Feb. 2017. https://doi.org/10.1186/s11671-017-1891-5

[81] D. Valerini, A. Cretì, A. P. Caricato, M. Lomascolo, R. Rella, and M. Martino, “Optical gas sensing through nanostructured ZnO films with different morphologies,” *Sensors and Actuators B: Chemical*, vol. 145, no. 1, pp. 167–173, Mar. 2010. https://doi.org/10.1016/j.snb.2009.11.064

[82] R. Aad, V. Simic, L. L. Cunff, L. Rocha, V. Sallet, C. Sartel, A. Lusson, C. Couteau, and G. Lerondel, “ZnO nanowires as effective luminescent sensing materials for nitroaromatic derivatives,” *Nanoscale*, vol. 5, no. 19, pp. 9176–9180, 2013. https://doi.org/10.1039/C3NR02416D

[83] J. R. Sanchez-Valencia, M. Alcaire, P. Romero-Gómez, M. Macias-Montero, F. J. Aparicio, A. Borras, A. R. Gonzalez-Elipe, and A. Barranco, "Oxygen Optical Sensing in Gas and Liquids with Nanostructured ZnO Thin Films Based on Exciton Emission Detection," *J. Phys. Chem. C*, vol. 118, no. 18, pp. 9852–9859, May 2014. https://doi.org/10.1021/jp5026027

[84] A. R. Gheisi, C. Neygandhi, A. K. Sternig, E. Carrasco, H. Marbach, D. Thomele, and O. Diwald, "O_2 adsorption dependent photoluminescence emission from metal oxide nanoparticles," *Physical Chemistry Chemical Physics*, vol. 16, no. 43, pp. 23922–23929, 2014. https://doi.org/10.1039/C4CP03080J

[85] X. Liu, Y. Sun, M. Yu, Y. Yin, B. Yang, W. Cao, and M. N. R. Ashfold, "Incident fluence dependent morphologies, photoluminescence and optical oxygen sensing properties of ZnO nanorods grown by pulsed laser deposition," *J. Mater. Chem. C*, vol. 3, no. 11, pp. 2557–2562, Mar. 2015. https://doi.org/10.1039/C4TC02924K

[86] M. Madel, J. Jakob, F. Huber, B. Neuschl, S. Bauer, Y. Xie, I. Tischer, and K. Thonke, "Optical gas sensing by micro-photoluminescence on multiple and single ZnO nanowires," *Phys. Status Solidi A*, vol. 212, no. 8, pp. 1810–1816, Aug. 2015. https://doi.org/10.1002/pssa.201431688

[87] P. Wang, T. Xie, L. Peng, H. Li, T. Wu, S. Pang, and D. Wang, "Water-Assisted Synthesis of Anatase TiO2 Nanocrystals: Mechanism and Sensing Properties to Oxygen at Room Temperature," *J. Phys. Chem. C*, vol. 112, no. 17, pp. 6648–6652, May 2008. https://doi.org/10.1021/jp800409f

[88] D. Pallotti, E. Orabona, S. Amoruso, P. Maddalena, and S. Lettieri, "Modulation of mixed-phase titania photoluminescence by oxygen adsorption," *Applied Physics Letters*, vol. 105, no. 3, p. 031903, Jul. 2014. https://doi.org/10.1063/1.4891038

[89] W. Shirbeeny and W. E. Mahmoud, "Synthesis and characterization of transparent optical gas sensor device made of indium oxide pyramid like nanoarchitectures," *Sensors and Actuators B: Chemical*, vol. 191, pp. 102–107, Feb. 2014. https://doi.org/10.1016/j.snb.2013.09.058

[90] S. Mochizuki and H. Araki, "Reversible photoinduced spectral transition in Eu2O3–γAl2O3 composites at room temperature," *Physica B: Condensed Matter*, vol. 340, no. Supplement C, pp. 913–917, Dec. 2003. https://doi.org/10.1016/j.physb.2003.09.204

[91] V. Reedo, S. Lange, V. Kiisk, A. Lukner, T. Tätte, and I. Sildos, "Influence of ambient gas on the photoluminescence of sol-gel derived TiO_2:Sm^{3+} films," presented at the Optical Materials and Applications, 2006, vol. 5946, p. 59460F. https://doi.org/10.1117/12.639162

[92] T. Tachikawa, T. Ishigaki, J.-G. Li, M. Fujitsuka, and T. Majima, "Defect-Mediated Photoluminescence Dynamics of Eu3+-Doped TiO2 Nanocrystals Revealed at the Single-Particle or Single-Aggregate Level," *Angewandte Chemie International Edition*, vol. 47, no. 29, pp. 5348–5352, Jul. 2008. https://doi.org/10.1002/anie.200800528

[93] N. A. F. Almeida, J. Rodrigues, P. Silva, N. Emami, M. J. Soares, T. Monteiro, J. A. Lopes-da-Silva, and P. A. A. P. Marques, "Pressure dependent luminescence in titanium dioxide particles modified with europium ions," *Sensors and Actuators B: Chemical*, vol. 234, no. Supplement C, pp. 137–144, Oct. 2016. https://doi.org/10.1016/j.snb.2016.04.157

[94] I. Aydin, K. Ertekin, S. Demirci, S. Gultekin, and E. Celik, “Sol-gel synthesized Sr4Al14O25:Eu2+/Dy3+ blue–green phosphorous as oxygen sensing materials,” *Optical Materials*, vol. 62, no. Supplement C, pp. 285–296, Dec. 2016. https://doi.org/10.1016/j.optmat.2016.10.019

[95] W. Tang, Y. Sun, S. Wang, B. Du, Y. Yin, X. Liu, B. Yang, W. Cao, and M. Yu, “Pr^{3+} -Doped ($K_{0.5}$ $Na_{0.5}$)NbO_3 as a high response optical oxygen sensing agent,” *J. Mater. Chem. C*, vol. 4, no. 48, pp. 11508–11513, 2016. https://doi.org/10.1039/C6TC04216C

[96] H. Weng, X.-Y. Xu, and B. Yan, “Novel multi-component photofunctional nano-hybrids for ratio-dependent oxygen sensing,” *Journal of Colloid and Interface Science*, vol. 502, no. Supplement C, pp. 8–15, Sep. 2017. https://doi.org/10.1016/j.jcis.2017.04.081

[97] L. Puust, V. Kiisk, M. Eltermann, H. Mändar, R. Saar, S. Lange, I. Sildos, Leonid Dolgov, L. Matisen, and R. Jaaniso, “Effect of ambient oxygen on the photoluminescence of sol–gel-derived nanocrystalline ZrO_2:Eu,Nb,” *J. Phys. D: Appl. Phys.*, vol. 50, no. 21, p. 215303, 2017. https://doi.org/10.1088/1361-6463/aa6c48

[98] S. K. Gupta, R. Desai, P. K. Jha, S. Sahoo, and D. Kirin, “Titanium dioxide synthesized using titanium chloride: size effect study using Raman spectroscopy and photoluminescence,” *J. Raman Spectrosc.*, vol. 41, no. 3, pp. 350–355, Mar. 2010. https://doi.org/10.1002/jrs.2427

[99] S. Lange, I. Sildos, V. Kiisk, and J. Aarik, “Energy transfer in the photoexcitation of Sm3+-implanted TiO2 thin films,” *Materials Science and Engineering: B*, vol. 112, no. 1, pp. 87–90, Sep. 2004. https://doi.org/10.1016/j.mseb.2004.06.007

[100] Y. Lei, L. D. Zhang, G. W. Meng, G. H. Li, X. Y. Zhang, C. H. Liang, W. Chen, and S. X. Wang, “Preparation and photoluminescence of highly ordered TiO2 nanowire arrays,” *Appl. Phys. Lett.*, vol. 78, no. 8, pp. 1125–1127, Feb. 2001. https://doi.org/10.1063/1.1350959

[101] T. Sekiya, M. Tasaki, K. Wakabayashi, and S. Kurita, “Relaxation process in anatase TiO2 single crystals with different colors,” *Journal of Luminescence*, vol. 108, no. 1, pp. 69–73, Jun. 2004. https://doi.org/10.1016/j.jlumin.2004.01.013

[102] C. C. Mercado, F. J. Knorr, J. L. McHale, S. M. Usmani, A. S. Ichimura, and L. V. Saraf, “Location of Hole and Electron Traps on Nanocrystalline Anatase TiO2,” *J. Phys. Chem. C*, vol. 116, no. 19, pp. 10796–10804, May 2012. https://doi.org/10.1021/jp301680d

[103] G. H. Dieke, *Spectra and Energy Levels of Rare Earth Ions in Crystals*. John Wiley & Sons, Ltd, 1968.

[104] A. M. Eppler, I. M. Ballard, and J. Nelson, “Charge transport in porous nanocrystalline titanium dioxide,” *Physica E: Low-dimensional Systems and Nanostructures*, vol. 14, no. 1, pp. 197–202, Apr. 2002. https://doi.org/10.1016/S1386-9477(02)00383-1

[105] K. Huang and Q. Zhang, “Giant Persistent Photoconductivity of the WO 3 Nanowires in Vacuum Condition,” *Nanoscale Res Lett*, vol. 6, no. 1, p. 52, Dec. 2011. https://doi.org/10.1007/s11671-010-9800-1

[106] Z. G. Yin, X. W. Zhang, Z. Fu, X. L. Yang, J. L. Wu, G. S. Wu, L. Gong, and P. K. Chu, “Persistent photoconductivity in ZnO nanostructures induced by surface oxygen vacancy,” *physica status solidi (RRL) – Rapid Research Letters*, vol. 6, no. 3, pp. 117–119, Mar. 2012. https://doi.org/10.1002/pssr.201105551

[107] D. B. Medved, “Photodesorption in Zinc Oxide Semiconductor,” *The Journal of Chemical Physics*, vol. 28, no. 5, pp. 870–873, May 1958. https://doi.org/10.1063/1.1744286
[108] D. Sporleder, D. P. Wilson, and M. G. White, “Final State Distributions of O2 Photodesorbed from TiO2(110),” *J. Phys. Chem. C*, vol. 113, no. 30, pp. 13180–13191, Jul. 2009. https://doi.org/10.1021/jp901065j
[109] T. Saidi, D. Palmowski, S. Babicz-Kiewlicz, T. G. Welearegay, N. El Bari, R. Ionescu, J. Smulko, and B. Bouchikhi, “Exhaled breath gas sensing using pristine and functionalized WO3 nanowire sensors enhanced by UV-light irradiation,” *Sensors and Actuators B: Chemical*, vol. 273, pp. 1719–1729, Nov. 2018. https://doi.org/10.1016/j.snb.2018.07.098
[110] M. C. Carotta, A. Cervi, A. Fioravanti, S. Gherardi, A. Giberti, B. Vendemiati, D. Vincenzi, and M. Sacerdoti, “A novel ozone detection at room temperature through UV-LED-assisted ZnO thick film sensors,” *Thin Solid Films*, vol. 520, no. 3, pp. 939–946, Nov. 2011. https://doi.org/10.1016/j.tsf.2011.04.173
[111] F. H. Saboor, T. Ueda, K. Kamada, T. Hyodo, Y. Mortazavi, A. A. Khodadadi, and Y. Shimizu, “Enhanced NO2 gas sensing performance of bare and Pd-loaded SnO2 thick film sensors under UV-light irradiation at room temperature,” *Sensors and Actuators B: Chemical*, vol. 223, pp. 429–439, Feb. 2016. https://doi.org/10.1016/j.snb.2015.09.075
[112] Ž. Antić, R. M. Krsmanović, M. G. Nikolić, M. Marinović-Cincović, M. Mitrić, S. Polizzi, and M. D. Dramićanin, “Multisite luminescence of rare earth doped TiO2 anatase nanoparticles,” *Materials Chemistry and Physics*, vol. 135, no. 2–3, pp. 1064–1069, Aug. 2012. https://doi.org/10.1016/j.matchemphys.2012.06.016
[113] W. Luo, R. Li, and X. Chen, “Host-Sensitized Luminescence of Nd3+ and Sm3+ Ions Incorporated in Anatase Titania Nanocrystals,” *J. Phys. Chem. C*, vol. 113, no. 20, pp. 8772–8777, May 2009. https://doi.org/10.1021/jp901862k
[114] A. Blumen and J. Manz, “On the concentration and time dependence of the energy transfer to randomly distributed acceptors,” *The Journal of Chemical Physics*, vol. 71, no. 11, pp. 4694–4702, Dec. 1979. https://doi.org/10.1063/1.438253
[115] A. Rose, “Space-Charge-Limited Currents in Solids,” *Phys. Rev.*, vol. 97, no. 6, pp. 1538–1544, Mar. 1955. https://doi.org/10.1103/PhysRev.97.1538
[116] E. Konstantinova, J. Weidmann, and T. Dittrich, “Influence of Adsorbed Water and Oxygen on the Photoluminescence and EPR of Por-TiO2 (Anatase),” *Journal of Porous Materials*, vol. 7, no. 1–3, pp. 389–392, Jan. 2000. https://doi.org/10.1023/A:1009699324013
[117] M. A. Henderson, “A surface science perspective on TiO2 photocatalysis,” *Surface Science Reports*, vol. 66, no. 6, pp. 185–297, Jun. 2011. https://doi.org/10.1016/j.surfrep.2011.01.001
[118] B. Weiler, A. Gagliardi, and P. Lugli, “Kinetic Monte Carlo Simulations of Defects in Anatase Titanium Dioxide,” *J. Phys. Chem. C*, vol. 120, no. 18, pp. 10062–10077, May 2016. https://doi.org/10.1021/acs.jpcc.6b01687

ACKNOWLEDGEMENTS

I would like to thank my supervisors Sven Lange and Raivo Jaaniso for their support throughout my studies. I am particularly grateful for Sven Lange's emphasis on understandibility and communication skills, values that are often underrated but are actually extremely useful both in and outside the academia. Raivo Jaaniso, on the other hand, has been an invaluable source of knowledge of optics, spectroscopy and gas sensing and has taught me to pay attention to intricate details while still keeping an eye on the broader picture.

I would also like to thank Valter Kiisk for useful ideas and support with experiments and Kathriin Utt for tutoring me through my first year in my PhD studies.

This work was supported by institutional research funding of the Estonian Ministry of Education and Research (project IUT34-27), by Estonian Science Foundation (project ETF9281) and by European Regional Development Fund (SA Archimedes projects 3.2.1101.12-0018 and 3.2.1101.12-0014).

PUBLICATIONS

CURRICULUM VITAE

Name	Marko Eltermann
Date of birth	1987-12-01
Citizenship	Estonian
Gender	male
E-mail	markoeltermann@gmail.com

Education

2012 – 2014	University of Tartu, MSc in physics
2007 – 2012	University of Tartu, BSc in physics
(2008 – 2009)	Conscription in the Estonian Defence Force
2004 – 2007	Tallinn Secondary Science School

Nimi	Marko Eltermann
Sünnikuupäev	1987-12-01
Kodakondsus	eestlane
E-mail	markoeltermann@gmail.com

Haridus

2012 – 2014	Tartu Ülikool, magistrikraad füüsikas
2007 – 2012	Tartu Ülikool, bakalaureusekraad füüsikas
(2008 – 2009)	Ajateenistus Kaitseväes
2004 – 2007	Tallinna Reaalkool

DISSERTATIONES PHYSICAE UNIVERSITATIS TARTUENSIS

1. **Andrus Ausmees.** XUV-induced electron emission and electron-phonon interaction in alkali halides. Tartu, 1991.
2. **Heiki Sõnajalg.** Shaping and recalling of light pulses by optical elements based on spectral hole burning. Tartu, 1991.
3. **Sergei Savihhin.** Ultrafast dynamics of F-centers and bound excitons from picosecond spectroscopy data. Tartu, 1991.
4. **Ergo Nõmmiste.** Leelishalogeniidide röntgenelektronemissioon kiiritamisel footonitega energiaga 70–140 eV. Tartu, 1991.
5. **Margus Rätsep.** Spectral gratings and their relaxation in some low-temperature impurity-doped glasses and crystals. Tartu, 1991.
6. **Tõnu Pullerits.** Primary energy transfer in photosynthesis. Model calculations. Tartu, 1991.
7. **Olev Saks.** Attoampri diapasoonis voolude mõõtmise füüsikalised alused. Tartu, 1991.
8. **Andres Virro.** AlGaAsSb/GaSb heterostructure injection lasers. Tartu, 1991.
9. **Hans Korge.** Investigation of negative point discharge in pure nitrogen at atmospheric pressure. Tartu, 1992.
10. **Jüri Maksimov.** Nonlinear generation of laser VUV radiation for high-resolution spectroscopy. Tartu, 1992.
11. **Mark Aizengendler.** Photostimulated transformation of aggregate defects and spectral hole burning in a neutron-irradiated sapphire. Tartu, 1992.
12. **Hele Siimon.** Atomic layer molecular beam epitaxy of A^2B^6 compounds described on the basis of kinetic equations model. Tartu, 1992.
13. **Tõnu Reinot.** The kinetics of polariton luminescence, energy transfer and relaxation in anthracene. Tartu, 1992.
14. **Toomas Rõõm.** Paramagnetic H^{2-} and F^+ centers in CaO crystals: spectra, relaxation and recombination luminescence. Tallinn, 1993.
15. **Erko Jalviste.** Laser spectroscopy of some jet-cooled organic molecules. Tartu, 1993.
16. **Alvo Aabloo.** Studies of crystalline celluloses using potential energy calculations. Tartu, 1994.
17. **Peeter Paris.** Initiation of corona pulses. Tartu, 1994.
18. **Павел Рубин.** Локальные дефектные состояния в CuO_2 плоскостях высокотемпературных сверхпроводников. Тарту, 1994.
19. **Olavi Ollikainen.** Applications of persistent spectral hole burning in ultrafast optical neural networks, time-resolved spectroscopy and holographic interferometry. Tartu, 1996.
20. **Ülo Mets.** Methodological aspects of fluorescence correlation spectroscopy. Tartu, 1996.
21. **Mikhail Danilkin.** Interaction of intrinsic and impurity defects in CaS:Eu luminophors. Tartu, 1997.

22. **Ирина Кудрявцева.** Создание и стабилизация дефектов в кристаллах KBr, KCl, RbCl при облучении ВУФ-радиацией. Тарту, 1997.
23. **Andres Osvet.** Photochromic properties of radiation-induced defects in diamond. Tartu, 1998.
24. **Jüri Örd.** Classical and quantum aspects of geodesic multiplication. Tartu, 1998.
25. **Priit Sarv.** High resolution solid-state NMR studies of zeolites. Tartu, 1998.
26. **Сергей Долгов.** Электронные возбуждения и дефектообразование в некоторых оксидах металлов. Тарту, 1998.
27. **Kaupo Kukli.** Atomic layer deposition of artificially structured dielectric materials. Tartu, 1999.
28. **Ivo Heinmaa.** Nuclear resonance studies of local structure in $RBa_2Cu_3O_{6+x}$ compounds. Tartu, 1999.
29. **Aleksander Shelkan.** Hole states in CuO_2 planes of high temperature superconducting materials. Tartu, 1999.
30. **Dmitri Nevedrov.** Nonlinear effects in quantum lattices. Tartu, 1999.
31. **Rein Ruus.** Collapse of 3d (4f) orbitals in 2p (3d) excited configurations and its effect on the x-ray and electron spectra. Tartu, 1999.
32. **Valter Zazubovich.** Local relaxation in incommensurate and glassy solids studied by Spectral Hole Burning. Tartu, 1999.
33. **Indrek Reimand.** Picosecond dynamics of optical excitations in GaAs and other excitonic systems. Tartu, 2000.
34. **Vladimir Babin.** Spectroscopy of exciton states in some halide macro- and nanocrystals. Tartu, 2001.
35. **Toomas Plank.** Positive corona at combined DC and AC voltage. Tartu, 2001.
36. **Kristjan Leiger.** Pressure-induced effects in inhomogeneous spectra of doped solids. Tartu, 2002.
37. **Helle Kaasik.** Nonperturbative theory of multiphonon vibrational relaxation and nonradiative transitions. Tartu, 2002.
38. **Tõnu Laas.** Propagation of waves in curved spacetimes. Tartu, 2002.
39. **Rünno Lõhmus.** Application of novel hybrid methods in SPM studies of nanostructural materials. Tartu, 2002.
40. **Kaido Reivelt.** Optical implementation of propagation-invariant pulsed free-space wave fields. Tartu, 2003.
41. **Heiki Kasemägi.** The effect of nanoparticle additives on lithium-ion mobility in a polymer electrolyte. Tartu, 2003.
42. **Villu Repän.** Low current mode of negative corona. Tartu, 2004.
43. **Алексей Котлов.** Оксианионные диэлектрические кристаллы: зонная структура и электронные возбуждения. Tartu, 2004.
44. **Jaak Talts.** Continuous non-invasive blood pressure measurement: comparative and methodological studies of the differential servo-oscillometric method. Tartu, 2004.
45. **Margus Saal.** Studies of pre-big bang and braneworld cosmology. Tartu, 2004.

46. **Eduard Gerškevitš.** Dose to bone marrow and leukaemia risk in external beam radiotherapy of prostate cancer. Tartu, 2005.
47. **Sergey Shchemelyov.** Sum-frequency generation and multiphoton ionization in xenon under excitation by conical laser beams. Tartu, 2006.
48. **Valter Kiisk.** Optical investigation of metal-oxide thin films. Tartu, 2006.
49. **Jaan Aarik.** Atomic layer deposition of titanium, zirconium and hafnium dioxides: growth mechanisms and properties of thin films. Tartu, 2007.
50. **Astrid Rekker.** Colored-noise-controlled anomalous transport and phase transitions in complex systems. Tartu, 2007.
51. **Andres Punning.** Electromechanical characterization of ionic polymer-metal composite sensing actuators. Tartu, 2007.
52. **Indrek Jõgi.** Conduction mechanisms in thin atomic layer deposited films containing TiO_2. Tartu, 2007.
53. **Aleksei Krasnikov.** Luminescence and defects creation processes in lead tungstate crystals. Tartu, 2007.
54. **Küllike Rägo.** Superconducting properties of MgB_2 in a scenario with intra- and interband pairing channels. Tartu, 2008.
55. **Els Heinsalu.** Normal and anomalously slow diffusion under external fields. Tartu, 2008.
56. **Kuno Kooser.** Soft x-ray induced radiative and nonradiative core-hole decay processes in thin films and solids. Tartu, 2008.
57. **Vadim Boltrushko.** Theory of vibronic transitions with strong nonlinear vibronic interaction in solids. Tartu, 2008.
58. **Andi Hektor.** Neutrino Physics beyond the Standard Model. Tartu, 2008.
59. **Raavo Josepson.** Photoinduced field-assisted electron emission into gases. Tartu, 2008.
60. **Martti Pärs.** Study of spontaneous and photoinduced processes in molecular solids using high-resolution optical spectroscopy. Tartu, 2008.
61. **Kristjan Kannike.** Implications of neutrino masses. Tartu, 2008.
62. **Vigen Issahhanjan.** Hole and interstitial centres in radiation-resistant MgO single crystals. Tartu, 2008.
63. **Veera Krasnenko.** Computational modeling of fluorescent proteins. Tartu, 2008.
64. **Mait Müntel.** Detection of doubly charged higgs boson in the CMS detector. Tartu, 2008.
65. **Kalle Kepler.** Optimisation of patient doses and image quality in diagnostic radiology. Tartu, 2009.
66. **Jüri Raud.** Study of negative glow and positive column regions of capillary HF discharge. Tartu, 2009.
67. **Sven Lange.** Spectroscopic and phase-stabilisation properties of pure and rare-earth ions activated ZrO_2 and HfO_2. Tartu, 2010.
68. **Aarne Kasikov.** Optical characterization of inhomogeneous thin films. Tartu, 2010.
69. **Heli Valtna-Lukner.** Superluminally propagating localized optical pulses. Tartu, 2010.

70. **Artjom Vargunin.** Stochastic and deterministic features of ordering in the systems with a phase transition. Tartu, 2010.
71. **Hannes Liivat.** Probing new physics in e+e− annihilations into heavy particles via spin orientation effects. Tartu, 2010.
72. **Tanel Mullari.** On the second order relativistic deviation equation and its applications. Tartu, 2010.
73. **Aleksandr Lissovski.** Pulsed high-pressure discharge in argon: spectroscopic diagnostics, modeling and development. Tartu, 2010.
74. **Aile Tamm.** Atomic layer deposition of high-permittivity insulators from cyclopentadienyl-based precursors. Tartu, 2010.
75. **Janek Uin.** Electrical separation for generating standard aerosols in a wide particle size range. Tartu, 2011.
76. **Svetlana Ganina.** Hajusandmetega ülesanded kui üks võimalus füüsikaõppe efektiivsuse tõstmiseks. Tartu, 2011
77. **Joel Kuusk.** Measurement of top-of-canopy spectral reflectance of forests for developing vegetation radiative transfer models. Tartu, 2011.
78. **Raul Rammula**. Atomic layer deposition of HfO_2 – nucleation, growth and structure development of thin films. Tartu, 2011.
79. **Сергей Наконечный.** Исследование электронно-дырочных и интерстициал-вакансионных процессов в монокристаллах MgO и LiF методами термоактивационной спектроскопии. Тарту, 2011.
80. **Niina Voropajeva.** Elementary excitations near the boundary of a strongly correlated crystal. Tartu, 2011.
81. **Martin Timusk.** Development and characterization of hybrid electro-optical materials. Tartu, 2012, 106 p.
82. **Merle Lust.** Assessment of dose components to Estonian population. Tartu, 2012, 84 p.
83. **Karl Kruusamäe.** Deformation-dependent electrode impedance of ionic electromechanically active polymers. Tartu, 2012, 128 p.
84. **Liis Rebane.** Measurement of the $W \to \tau\nu$ cross section and a search for a doubly charged Higgs boson decaying to τ-leptons with the CMS detector. Tartu, 2012, 156 p.
85. **Jevgeni Šablonin.** Processes of structural defect creation in pure and doped MgO and NaCl single crystals under condition of low or super high density of electronic excitations. Tartu, 2013, 145 p.
86. **Riho Vendt**. Combined method for establishment and dissemination of the international temperature scale. Tartu, 2013, 108 p.
87. **Peeter Piksarv.** Spatiotemporal characterization of diffractive and non-diffractive light pulses. Tartu, 2013, 156 p.
88. **Anna Šugai.** Creation of structural defects under superhigh-dense irradiation of wide-gap metal oxides. Tartu, 2013, 108 p.
89. **Ivar Kuusik.** Soft X-ray spectroscopy of insulators. Tartu, 2013, 113 p.
90. **Viktor Vabson**. Measurement uncertainty in Estonian Standard Laboratory for Mass. Tartu, 2013, 134 p.

91. **Kaupo Voormansik.** X-band synthetic aperture radar applications for environmental monitoring. Tartu, 2014, 117 p.
92. **Deivid Pugal.** hp-FEM model of IPMC deformation. Tartu, 2014, 143 p.
93. **Siim Pikker.** Modification in the emission and spectral shape of photostable fluorophores by nanometallic structures. Tartu, 2014, 98 p.
94. **Mihkel Pajusalu**. Localized Photosynthetic Excitons. Tartu, 2014, 183 p.
95. **Taavi Vaikjärv.** Consideration of non-adiabaticity of the Pseudo-Jahn-Teller effect: contribution of phonons. Tartu, 2014, 129 p.
96. **Martin Vilbaste.** Uncertainty sources and analysis methods in realizing SI units of air humidity in Estonia. Tartu, 2014, 111 p.
97. **Mihkel Rähn.** Experimental nanophotonics: single-photon sources- and nanofiber-related studies. Tartu, 2015, 107 p.
98. **Raul Laasner.** Excited state dynamics under high excitation densities in tungstates. Tartu, 2015, 125 p.
99. **Andris Slavinskis.** EST Cube-1 attitude determination. Tartu, 2015, 104 p.
100. **Karlis Zalite**. Radar Remote Sensing for Monitoring Forest Floods and Agricultural Grasslands. Tartu, 2016, 124 p.
101. **Kaarel Piip.** Development of LIBS for *in-situ* study of ITER relevant materials. Tartu, 2016, 93 p.
102. **Kadri Isakar.** ^{210}Pb in Estonian air: long term study of activity concentrations and origin of radioactive lead. Tartu, 2016, 107 p.
103. **Artur Tamm.** High entropy alloys: study of structural properties and irradiation response. Tartu, 2016, 115 p.
104. **Rasmus Talviste.** Atmospheric-pressure He plasma jet: effect of dielectric tube diameter. Tartu, 2016, 107 p.
105. **Andres Tiko.** Measurement of single top quark properties with the CMS detector. Tartu, 2016, 161 p.
106. **Aire Olesk.** Hemiboreal Forest Mapping with Interferometric Synthetic Aperture Radar. Tartu, 2016, 121 p.
107. **Fred Valk.** Nitrogen emission spectrum as a measure of electric field strength in low-temperature gas discharges. Tartu, 2016, 149 p.
108. **Manoop Chenchiliyan.** Nano-structural Constraints for the Picosecond Excitation Energy Migration and Trapping in Photosynthetic Membranes of Bacteria. Tartu, 2016, 115p.
109. **Lauri Kaldamäe.** Fermion mass and spin polarisation effects in top quark pair production and the decay of the higgs boson. Tartu, 2017, 104 p.
110. **Marek Oja.** Investigation of nano-size α- and transition alumina by means of VUV and cathodoluminescence spectroscopy. Tartu, 2017, 89 p.
111. **Viktoriia Levushkina.** Energy transfer processes in the solid solutions of complex oxides. Tartu, 2017, 101 p.
112. **Mikk Antsov.** Tribomechanical properties of individual 1D nanostructures: experimental measurements supported by finite element method simulations. Tartu, 2017, 101 p.
113. **Hardi Veermäe.** Dark matter with long range vector-mediated interactions. Tartu, 2017, 137 p.

114. **Aris Auzans.** Development of computational model for nuclear energy systems analysis: natural resources optimisation and radiological impact minimization. Tartu, 2018, 138 p.
115. **Aleksandr Gurev**. Coherent fluctuating nephelometry application in laboratory practice. Tartu, 2018, 150 p.
116. **Ardi Loot**. Enhanced spontaneous parametric downconversion in plasmonic and dielectric structures. Tartu, 2018, 164 p.
117. **Andreas Valdmann.** Generation and characterization of accelerating light pulses. Tartu, 2019, 85 p.
118. **Mikk Vahtrus.** Structure-dependent mechanical properties of individual one-dimensional metal-oxide nanostructures. Tartu, 2019, 110 p.
119. **Ott Vilson.** Transformation properties and invariants in scalar-tensor theories of gravity. Tartu, 2019, 183 p.
120. **Indrek Sünter.** Design and characterisation of subsystems and software for ESTCube-1 nanosatellite. Tartu, 2019, 195 p.